Brain FGF2 and NCAM1 contribute to FGFR1-dependent progression of ER+ breast cancer brain metastases in young and aged hosts

Authors: Morgan S. Fox[1], Jenny A. Jaramillo-Gómez[1], R. Alejandro Marquez-Ortiz[1], Karen L.F. Alvarez-Eraso[1], Maria J. Contreras-Zárate[1], Trinh C. Pham[1], Elaina N. Barela[1], Stella N. Koliavas[1], Peter Kabos[2,4], Natalie J. Serkova[3,4], Carol A. Sartorius[1,4], Elizabeth A. Wellberg[5], Diana M. Cittelly[*1,4]

Affiliations: [1]Department of Pathology; [2]Department of Medicine, Division of Medical Oncology; [3]Department of Radiology, Animal Imaging Shared Resource; [4]University of Colorado Comprehensive Cancer Center, University of Colorado Anschutz, Aurora, CO, 80045, USA. [5]Department of Pathology, Harold Hamm Diabetes Center, and Stephenson Cancer Center, University of Oklahoma Health Sciences Center, Oklahoma City, OK, USA.

Contact Information: Diana M. Cittelly Ph.D. 12801 E 17th Ave. University of Colorado Anschutz, Aurora, CO, 80045. Diana.Cittelly@cuanschutz.edu

ABSTRACT

Estrogen receptor positive (ER+) breast cancer represents a significant proportion of breast cancer brain metastasis but remains understudied. Here, we report that FGFR1-amplification, a well-established driver of ER+ breast cancer endocrine resistance, promotes ER+ breast cancer brain metastatic colonization in young and aged female mice, through both canonical FGF2/FGFR1 signaling and non-canonical NCAM1/FGFR1 interactions. Astrocytic FGF2-mediated paracrine activation of FGFR1 promoted breast cancer brain metastasis in estrogen-treated young mice, but FGF2 levels and signaling decreased in the brain with aging and estrogen-depletion. Neuronal and astrocytic NCAM1, which remain unchanged in young and aged brains, promoted adhesion to neurons, migration, and growth of ER+ cells, suggesting that interactions with astrocytes and neurons facilitate early ER+ breast cancer brain metastasis colonization through FGFR1. Importantly, FDA-approved FGFR inhibitors effectively blocked early colonization but not late-stage brain metastases, suggesting prevention of FGFR1+ brain metastases as a window of opportunity for FGFR1 inhibitors.

INTRODUCTION

The management of breast cancer brain metastases (BCBM) has emerged as a critical need for metastatic breast cancer (BC) patients[1]. Once diagnosed, brain metastases (BM) remain incurable, and more than 80% of patients die within one year of their diagnosis[2,3]. While BCBM show increased incidence in HER2+ and triple-negative (TNBC, lacking estrogen-receptor (ER), progesterone receptor (PR) and HER2 amplification) subtypes, up to 16% of patients with metastatic ER+ BC develop BM, and represent a large fraction of patients living with BCBM[4-6].

ER+ BC is effectively treated with anti-estrogen therapies, yet metastatic ER+ BC commonly arises in older women with tumors refractory to these therapies[5]. ER+ BCBM remains understudied, partly due to the dearth of ER+ mouse models that acquire estrogen (17β-estradiol, E2) independence and express drivers of endocrine resistance observed in humans[7-9]. Although human-derived ER+ transplantable tumors and cell lines (patient-derived xenografts, PDXs) are broadly used to study ER+ BC, their growth in mice requires supplementation with E2 mimicking premenopausal levels, as opposed to more relevant post-menopausal or post-endocrine therapy E2 levels in women[7,8,10-12]. Here, we demonstrate that the aged tumor microenvironment (TME) supports the progression of ER+ BC cells in the absence of E2-supplementation, providing clinically relevant models that mimic the natural progression of metastatic ER+ BC.

Mechanisms of acquired and innate resistance to anti-estrogens in ER+ BC have been the focus of extensive research; yet how specific niches at metastatic sites contribute to endocrine resistance and metastatic recurrence are less understood. FGFR1-amplification was recently reported as the only genomic alteration associated with increased risk of late recurrence in post-menopausal women with ER+ early BC on aromatase inhibitor therapy[13]. Aberrations in FGFR signaling have emerged as critical predictors of metastatic progression in ER+ BC following endocrine therapies[13-18]. A recent study showed that ER+ breast tumors acquire an FGFR4-associated signature that correlated with worse prognosis and provided significant and independent prognostic information for brain, liver, and lung metastasis in ER+ tumors only[15], and suggested that microenvironmental features (either growth factors or specific cell-cell contact) may facilitate growth at metastatic sites. FGFR1 aberrations are

53 significantly higher in BCBM patients compared to non-BM in metastatic BC and predicted poor
54 prognosis[19], further suggesting that FGFR1 may play a specific role in BCBM promotion.

55 Tyrosine kinase receptor amplification often results in ligand-independent autoactivation; however,
56 FGFR1-amplification alone is insufficient to drive E2-independent growth in models of ER+ BC primary
57 tumors[20]. In the brain, FGFR1 plays known roles in development and is implicated in synaptic repair
58 and maintenance[21-28]. Although FGFRs typically signal through their cognate FGF ligands, FGFR1 also
59 binds the neural cell adhesion molecule (NCAM), which is abundantly expressed on the surface of
60 neurons and glial cells, and has been shown to activate FGFR1 signaling and regulate synaptic
61 plasticity[21,29-37]. Here, we demonstrate that FGFR1 amplification confers a context-dependent
62 advantage to ER+ BC cells by enhancing brain seeding and outgrowth through microenvironmental
63 activation rather than cell-intrinsic receptor autophosphorylation. ER+ FGFR1+ cells have increased
64 ability to colonize the brain in young and aged/E2-suppressed mice, both through canonical
65 FGF2/FGFR1 signaling and non-canonical NCAM1/FGFR1 signaling. We show that canonical
66 FGF2/FGFR1 signaling decreases in the brain with aging and E2-depletion, and that astrocyte-derived
67 FGF2 drives FGFR1-dependent early brain colonization in young hosts, while NCAM1 serves as a non-
68 canonical FGFR1 activator that promotes brain colonization under aged, low-FGF2 conditions.
69 Importantly, paracrine activation of FGFR1 is critical for early brain colonization but not late-stage brain
70 metastases, suggesting a window of opportunity for FGFR inhibitors to block early colonization in
71 women at high risk of BM.

RESULTS

ER+ BCBM models recapitulate clinical progression of ER+ BC metastases throughout the lifespan

Analysis of BCBM samples showed that 41/85 (48.2%) originated from ER+ primary BC, with only 14/41 (34.1%) also harboring HER2-amplification (ER+ HER2+), suggesting that the majority of ER+ BCBM are not driven by HER2-amplification (**Fig. 1a**). Patients with ER+ BCBM were primarily postmenopausal at BM diagnosis, either due to age (>50 years) or prior endocrine therapy (**Fig. 1b,c**). Given the lack of ER+ BC models capable of spontaneous brain colonization, we determined the brain-homing ability of ER+ BC cells following hematogenous dissemination. Four BC PDX-derived cell lines[38] were injected intracardially in young (<12 weeks) female mice, supplemented with E2 to mimic premenopausal human levels[10] and required to drive ER+ BC growth in mice[39]. These cells colonized multiple organs, with brain colonization in 0% (UCD46), 20% (UCD4), 40% (UCD12), and 80% (UCD65) (**Fig. 1d**). Since the majority of ER+ BCBM develops following endocrine therapies, we next determined whether ER+ cells could spontaneously disseminate and outgrow upon endocrine therapy/E2-depletion. For this, we implanted UCD4 or UCD65 cells in the mammary fat pad of young ovariectomized (OVX) female NSG mice supplemented with E2 and allowed tumors to grow until reaching 1 cm^3 to mimic E2-dependent dissemination. Upon tumor removal, mice were randomized into 1) continued E2 supplementation (E2, mimicking E2-dependent metastatic progression in younger women); 2) E2 withdrawal (EWD, mimicking ovarian suppression in younger women); and 3) EWD + letrozole (mimicking full E2-depletion used in post-menopausal women) (**Supplementary Fig. 1a,f**). UCD4 remained E2-dependent for brain and extracranial growth and for dissemination to the brain and other organs (**Supplementary Fig. 1b-e**). BCBM continued growing in a subset of EWD mice, with macrometastasis incidence of 22.2% in the EWD group and 11% in the EWD+LET group. By contrast, E2 did not promote growth of spontaneously disseminated UCD65 cells in the brain but supported growth extracranially (**Supplementary Fig. 1g,h**). While E2 and EWD+LET-treated mice all showed evidence of disseminated UCD65 cells in the brain, mice succumbed to primary tumor recurrence or extracranial metastases (**Supplementary Fig. 1i,j**). Thus, these models fully recapitulate spontaneous

99 ER+ BC metastasis and provide evidence that ER+ BCBM emerge under E2-depletion conditions *in*
100 *vivo.*

101 Given the low BM outgrowth in spontaneous metastases models which prevents mechanistic studies,
102 we used intracardiac injection, mimicking early events of brain colonization, to determine the BM
103 capability of UCD65 cells in young or aged mice (**Fig. 1e**). Consistent with the known E2-dependence
104 of ER+ cells in young mice (<12 weeks), young OVX+ E2 injected with UCD65 cells showed increased
105 extracranial and brain metastasis, with 100% (13/13) mice showing histological evidence of
106 intraparenchymal BM compared to 50% (7/14) in OVX mice. However, in aged mice (>52 weeks), BM
107 were detected in 77% (10/13) and extracranial metastases outgrew in 100% of mice despite low
108 endogenous E2 (**Fig. 1f-h**). BM colonization in aged mice was not dependent on low levels of ovarian
109 E2 as UCD65 cells showed similar progression of BM and extracranial metastases in OVX or naïve
110 aged mice, with histological evidence of intraparenchymal BM in 82% (9/11) and 80% (8/10),
111 respectively (**Fig. 1i-l**). Histological quantification and MRI analysis of young and aged mice harboring
112 UCD65 BMs confirmed the presence of both intraparenchymal micrometastases and macrometastases
113 in both aged groups (**Fig. 1h,m, Supplementary Fig. 1k,l**). Furthermore, histological clusters correlate
114 with head bioluminescence (BLI) signal measured by IVIS (**Supplementary Fig. 1m**). Thus, ER+ BC
115 cells can grow in high E2/young hosts and in low E2/aged hosts.

116 **FGFR1 drives growth of ER+ BC in the brain TME *ex vivo***

117 As FGFR1-amplification has been reported as the only genomic alteration that predicts increased risk
118 of late metastatic recurrence in anti-estrogen-treated ER+ BC[13], we interrogated FGFR1 status in ER+
119 BCBM clinical samples and cells. Immunohistochemistry showed normal or high FGFR1 expression
120 that did not correlate with membrane pFGFR1 status in ER+ BCBM (**Fig. 2a**). ER+ cells with increased
121 brain-colonization ability (UCD12 and UCD65) harbor genomic amplification and increased FGFR1
122 mRNA and protein expression compared to the low and non-brain metastatic UCD4, UCD46, and
123 MCF7 cells (**Fig. 2b,c**). FGFR1 amplification in cell lines was not accompanied by increased
124 autophosphorylation (**Fig. 2c**) or expression of cognate FGFR1-activating ligands (**Supplementary Fig.**

125 **2a**), suggesting that FGFR1 function may depend on ligand-dependent activation through the TME
126 rather than auto-activation due to high receptor expression.

127 To determine how FGFR1 impacts growth of ER+ BC cells, we stably expressed non-targeting control
128 (shNC) or FGFR1-targeting shRNAs in UCD12 and UCD65 cells (**Fig. 2d, Supplementary Fig. 2b-e**).
129 shFGFR1 and shNC cells showed similar growth in E2-deprived media (vehicle) and in response to E2
130 in 2D culture (**Fig. 2e,f**). However, when cells were grown as spheroids and plated on organotypic brain
131 slices from young and aged mice, shFGFR1 UCD12 and UCD65 cells showed decreased ability to
132 survive and grow compared to shNC cells (**Fig. 2g-k**). Furthermore, FGFR1-overexpression in MCF7
133 cells (**Fig. 2l**) did not alter 2D cell growth under E2-deprived or E2-treated conditions compared to
134 empty vector (EV) control cells, but promoted growth in co-culture with organotypic brain slices from
135 young and aged mice (**Fig. 2m-o**). Thus, FGFR1 is a key mediator of survival and growth of ER+ BC
136 cells in the young and aged brain TME.

137 **FGFR1 promotes BCBM colonization of ER+ cells in the young and aged brain TME**

138 To test how FGFR1 impacted brain colonization *in vivo,* we intracardially injected shNC or shFGFR1
139 UCD65 cells into young OVX mice supplemented with E2 (**Fig. 3a**). FGFR1 knockdown (KD)
140 decreased BCBM progression and the number of intraparenchymal metastases but did not affect E2-
141 driven growth of extracranial metastasis (**Fig. 3b-d**). Injection of shNC or shFGFR1 UCD65 in naïve
142 aged mice showed that FGFR1 downregulation decreased BCBM progression, the number of
143 intraparenchymal metastases, and extracranial metastases (**Fig. 3e-h**). Similarly, FGFR1 KD in UCD12
144 decreased BCBM progression in aged naïve mice and delayed the outgrowth of extracranial metastasis
145 (**Fig. 3i-l**). Moreover, FGFR1-KD cells showed decreased brain signal (but not extracranial signal)
146 immediately following injection (Week 0) in aged mice (**Fig. 3f,j**), suggesting impaired seeding in the
147 aged brain parenchyma. To test if FGFR1 overexpression is sufficient to drive BM colonization and
148 outgrowth, EV or FGFR1-OE MCF7 cells were injected in young/E2 supplemented NSG mice. Despite
149 the poor brain -metastatic ability of MCF7 cells, FGFR1-OE increased BM progression and BM
150 incidence in young OVX + E2 (3/8, 38%) mice compared to OVX- mice (1/8, 12.5%) without impacting
151 E2-driven extracranial metastasis (**Supplementary Fig. 3a-d**). In aged mice, FGFR1-OE cells formed

152 BMs in 14.3% (1/7) mice while EV-MCF-7 cells were unable to colonize (0/8 mice) (**Supplementary**
153 **Fig. 3e,f**).Together, these data demonstrate that FGFR1 is a key driver of BCBM progression in the
154 young/E2-high TME and promotes brain colonization and extracranial metastases in aged mice.

155 **FGF2/FGFR1 signaling in glial cells decreases upon E2 suppression and aging.**

156 We next interrogated whether host age impacts FGFR1+ ER+ BCBM transcriptional profiles.
157 NanoString GeoMx Digital Spatial Profiling (DSP) followed by UMAP dimension reduction analysis
158 demonstrated no significant differences in the global transcriptional profiles of UCD65 BMs following 6
159 months of growth in young versus aged sham-mice, suggesting that late-stage ER+ BCBM are
160 transcriptionally similar, independent of host age. Pairwise comparisons revealed only six differentially
161 expressed genes between tumors in young and aged hosts, and Gene Set Enrichment Analysis
162 (GSEA) showed no significant pathway enrichment (**Fig. 4a-e, Supplementary Fig. 4**). To investigate
163 whether changes in the surrounding brain TME due to aging or ovariectomy may impact FGFR1
164 function in ER+ BCBM, GFAP+ and Iba+ glial areas surrounding PanCK+ UCD65 BMs were analyzed
165 using the mouse whole-transcriptome atlas (**Fig. 4f,g**). Dimension reduction analysis using global
166 transcriptomic profiles showed that glial cells surrounding BMs clustered by age and OVX status, with
167 OVX being a major driver of transcriptional changes and inducing aging-related profiles in young mice
168 (**Fig. 4h**). Pairwise comparisons further demonstrated that E2-depletion and aging broadly repressed
169 gene expression (**Fig. 4i**). To visualize the most representative biological patterns, we performed GSEA
170 and clustered outputs based on shared genes, which identified FGF/FGFR signaling as common top
171 pathways downregulated by OVX and aging (**Fig. 4j-l, Supplementary Data 1**). *Fgf2*, encoding the
172 canonical FGFR1 ligand, was among the top 20 common downregulated genes with OVX and aging
173 (**Fig. 4i,m,n, Supplementary Data 2**), suggesting that paracrine activation of FGFR1 in ER+ BCBM
174 may be driven by glial FGF2 in young hosts, and decreases with aging and E2-depletion.

175 **Astrocytes promote FGF2-dependent activation and proliferation of FGFR1+ ER+ BC cells**

176 We next explored how cells in the brain TME drive canonical FGFR1 activation in young and aged
177 hosts. Consistent with NanoString analysis, FGF2 protein levels were significantly lower in total brain,

178 oligodendrocytes, neurons, and astrocytes from tumor-naïve aged compared to young mice and in
179 astrocytes aged long-term (>3 months) *in vitro* (**Fig. 5a-c**). Since astrocytes expressed the highest
180 FGF2 levels in the brain, we first tested how astrocytic FGF2 impacted FGFR1-dependent ER+ BC
181 growth. UCD65 cells showed increased pFGFR1 when co-cultured with young and aged astrocytes in
182 E2-free media, but activation was higher with young astrocytes (**Fig. 5d**). E2-independent growth of
183 UCD65 cells was higher in co-culture with young astrocytes than with aged astrocytes, and FGFR1 KD
184 significantly decreased growth in co-culture with both young and aged astrocytes (**Fig. 5e-g**). Thus,
185 age-induced changes in astrocytic FGF2 levels correlate with increased FGFR1 activation and growth
186 in ER+ BC, which diminishes with astrocyte age. Similarly, co-culture with young human primary
187 astrocytes promoted UCD12 and UCD65 cell growth and was sensitive to FGFR1 downregulation
188 (**Supplementary Fig. 5a,b),** and blocking FGF2 with a neutralizing antibody decreased UCD12
189 spheroid growth in organotypic co-culture with young brain slices (**Fig. 5h,i**), suggesting that astrocytic-
190 dependent growth of ER+ BC cells is in part mediated by FGF2/FGFR1 signaling. Consistent with
191 studies showing FGF2 is heparin-bound on the cell membrane rather than secreted[40-42], FGF2 was not
192 detected in serum-free conditioned media from astrocytes (CM-Ast) but was membrane bound in
193 astrocytes co-cultured with UCD12 cells (**Supplementary Fig. 5c,d**). Moreover, CM-Ast-induced Akt
194 and ERK activation were not altered by BGJ398, a selective FGFR inhibitor that blocks FGF2-mediated
195 signaling and decreases FGF2-dependent proliferation in ER+ BC cells (**Supplementary Fig. 5e,f**).
196 Together, these results suggest that FGFR1 activation by membrane-bound FGF2 is critical for tumor
197 proliferation in the absence of exogenous E2, and that young but not aged astrocytes can robustly
198 support E2-independent proliferation of FGFR1+ BC cells.

199 **NCAM1 and FGF2 activate FGFR1 signaling and growth in ER+ BC**

200 Given that brain FGF2 levels decrease with age and E2-suppression, and aged astrocytes were less
201 effective in promoting FGFR1-dependent growth, we investigated whether non-canonical mechanisms
202 of FGFR1 function could impact ER+ BCBM in the absence of high FGF2. NCAM1 is a neuronal and
203 astrocytic cell adhesion molecule whose expression is unchanged with aging (**Supplementary Fig. 6a-**
204 **d**) and is known to activate FGFR1 and regulate neural development and synaptic plasticity[31,37,43-45]. To

205 determine if NCAM1 could activate FGFR1 kinase signaling in ER+ BC cells, we treated UCD65 cells
206 with NCAM1 and found dose-dependent activation of FGFR1, Akt, and ERK (**Fig. 6a**), even at the
207 lowest dose (which is below reported NCAM1 cell surfaces levels in the brain[31,32]). NCAM1-induced
208 signaling is dependent on FGFR1 expression, as it was decreased in shFGFR1 compared to shNC
209 UCD65, and only observed in MCF7-FGFR1-OE but not MCF7-EV cells (**Fig. 6b,c**). BGJ398 blocked
210 FGF2 and NCAM1-induced FGFR1 signaling in UCD65, UCD12, and MCF7-FGFR1-OE at multiple
211 time points (**Fig. 6d-f, Supplementary Fig. 6e,f**). Since NCAM1 is mostly membrane-anchored, we
212 next tested whether surface NCAM1 from neighboring cells activates FGFR1 by co-culturing ER+ BC
213 cells with NCAM1+ SY5Y neuroblastoma cells stably expressing shEV or shNCAM1. Co-culture with
214 shNCAM1 SY5Y cells significantly reduced FGFR1 phosphorylation in all ER+ cell lines compared to
215 shEV controls (**Fig. 6g,h, Supplementary Fig. 6g,h**). Similarly, co-culture with astrocytes transduced
216 with mCherry-tagged AAV expressing shNCAM1 reduced pFGFR1 in UCD65 and UCD12 cells
217 compared to EV control, demonstrating that NCAM1 from both neurons and astrocytes can activate
218 FGFR1 in ER+ BC cells (**Fig 6i,j, Supplementary Fig. 6i**). A blocking antibody against NCAM1
219 decreased UCD12 spheroid growth in aged, but not young organotypic brain slices, suggesting that
220 NCAM1 promotes growth of ER+ BC in the aged/low FGF2 brain TME, but it is not the main driver in
221 the high FGF2 young TME (**Fig. 6k,l**). Because young astrocytes express both NCAM1 and FGF2 at
222 high levels, we next examined their relative contribution to ER+ BC proliferation. Lentiviral-mediated KD
223 of NCAM1 and FGF2 effectively decreased FGF2 and NCAM1 levels in astrocytes, resulting in
224 significant decreased proliferation of UCD12 and UCD65 cells compared to co-culture with shNC
225 astrocytes. Astrocytic FGF2 KD produced a greater reduction in ER+ BC growth than NCAM1 KD, with
226 minimal additive effects upon combined depletion of NCAM1 and FGF2 (**Fig. 6m,n, Supplementary**
227 **Fig. 6j,k**). Thus, these results indicate that while astrocyte-derived FGF2 remains the dominant driver
228 of FGFR1-dependent growth in young brains, NCAM1 serves as a non-canonical FGFR1 activator that
229 sustains ER^+ BC growth under aged, low-FGF2 conditions.

230 **NCAM1/FGFR1 communication drives interactions between ER+ BC and neurons**

231 Studies have shown that FGF2 and NCAM1 activation of FGFR1 can result in different downstream
232 cellular effects[44]. To define downstream mechanisms resulting from NCAM1 or FGF2-mediated FGFR1
233 activation in ER+ BC cells, we performed global gene expression profiling of UCD12 and UCD65 cells
234 treated with vehicle, NCAM1, or FGF2 for 24h (**Fig. 7a, Supplementary Fig. 7a-c**). GSEA identified
235 gene signatures shared by both cell lines that were commonly enriched or repressed by NCAM1 and
236 FGF2 or uniquely regulated by each ligand (**Fig. 7b, Supplementary Data 3**). FGF2 and NCAM1
237 commonly induced 1,390 gene signatures, primarily clustered as signaling associated with
238 development and disease, DNA replication, and immunity. FGF2 induced 2,879 unique differential
239 signatures, demonstrating enrichment of canonical growth factor receptor signaling, cytoskeleton
240 organization, ECM interactions, and transmembrane transport and secretion (**Supplementary Fig.
241 7d,e, Supplementary Data 4,5**). By contrast, NCAM1 treatment induced 90 unique differential gene
242 signatures, primarily classified by disease and cell signaling activation, metabolic changes,
243 transmembrane transport, and, interestingly, neuronal gene signatures (**Fig. 7c, Supplementary Fig.
244 7f,g**). These neural signatures showed enrichment in differentiation, development, and adhesion, with
245 repression of postsynaptic membrane protein localization and trafficking, and
246 myelination/ensheathment (**Fig. 7d**). Therefore, these results suggest that FGF2 promotes broad
247 transcriptional changes, driving canonical signaling through FGFR1 and proliferation, while NCAM1
248 may drive specific gene signatures promoting neural interactions in ER+ BC cells.

249 Given the known roles of NCAM/FGFR1 interactions in modulating synaptic plasticity, the induction of
250 synaptic-related gene signatures upon NCAM1 treatment in UCD65 and UCD12 cells, and emerging
251 evidence that direct and indirect synaptic communication between neurons and disseminated brain
252 metastatic cells are key mediators of BCBM outgrowth[46-48], we next determined how FGFR1 impacts
253 cancer-neuron interactions. FGFR1 KD resulted in decreased density of excitatory synapses at the
254 interface of UCD65 spheroids and organotypic brain slices, suggesting that FGFR1 contributes to
255 synaptic localization or interaction between ER+ BC cells and organotypic brain slices (**Fig. 7e**).
256 Furthermore, coculture with primary hippocampal neurons from postnatal mice demonstrated that ER+
257 BC cells bind and migrate along neurites *in vitro*, and FGFR1 KD significantly decreased the distance

258 migrated by UCD65 and UCD12 cells along these neurites (**Fig. 7f,g**). NCAM1 KD in SY5Y cells
259 decreased migration of UCD65 and UCD12 cells in co-culture (**Fig. 7h**). Together, these results
260 suggest that FGFR1 promotes neuronal interactions and that FGFR1/NCAM1 facilitates migration of
261 ER+ BC cells.

262 **FGFR1 kinase inhibition is effective only in the prevention of ER+ BCBM**

263 Our data suggests that paracrine activation of FGFR1 by FGF2 and NCAM1 can influence early
264 colonization as well as late metastatic progression of ER+ BC. Since interactions with astrocytes and
265 neurons occur from early stages of metastatic colonization, we assessed UCD65 FGFR1 activation 5
266 days following intracardiac injection in young and aged hosts. Membrane pFGFR1 expression was
267 found in 83% of early disseminated cells in young mice and 57% in aged mice, and membrane
268 pFGFR1 intensity was stronger in disseminated cells in young compared to aged brains (**Fig. 8a,b**).
269 These findings are consistent with strong FGF2-dependent FGFR1 activation of disseminated cancer
270 cells in young mice, and weaker, NCAM-dependent activation in aged mice. In contrast, late-stage
271 UCD65 BCBM from young and aged mice showed minimal membrane pFGFR1 (**Fig. 8c**), paralleling
272 the lack of correlation between pFGFR1 status and total FGFR1 expression observed in late-stage
273 clinical samples (**Fig. 2a**). Thus, this data suggests that paracrine activation of FGFR1 is prominent
274 during early brain colonization, but it is dispensable during later stages of BM progression. To test this,
275 we injected UCD65 cells in young mice supplemented with E2 or in aged naïve mice (**Fig. 8d,i**) and
276 began treatment with vehicle or BGJ398 either immediately after injection or upon detectable brain
277 metastatic outgrowth. We confirmed the reported brain-penetrance of BGJ398[49], as it effectively
278 blocked TME-mediated FGFR1 activation in disseminated cancer cells at the dose used
279 (**Supplementary Fig. 8a**). In young mice, early FGFR inhibition significantly suppressed BCBM
280 progression, reducing IVIS-detectable BM as well as the number of micrometastases and BM clusters
281 when treatment was initiated at the time of cell injection, but not when initiated 7 weeks post-injection
282 (**Fig. 8e-h).** Consistent with the FGFR1 independence of advanced lesions, IF analysis revealed no
283 significant differences in pERK staining in late-stage BMs following BGJ398 treatment (**Supplementary**
284 **Fig. 8c,d**). In aged mice, characterized by weaker FGFR1 activation and slower BM progression,

285 BGJ398 treatment did not significantly affect BM progression or *ex vivo* IVIS (**Fig. 8j,k**), nor did it affect
286 extracranial progression (**Supplementary Fig. 8e**). Although BGJ398-associated toxicity in aged mice
287 required the termination of these studies before control mice reached euthanasia criteria, histological
288 quantification of BMs revealed that early treatment BGJ398 reduced the total number of metastatic
289 clusters and micrometastases (**Fig. 8l**). These findings support a role for FGFR1 activation in early
290 brain colonization, even in the aged brain, while suggesting that established metastases are largely
291 FGFR1-independent.

292 Together, our data suggests a model whereby FGF2 and NCAM1-dependent FGFR1 activation of
293 disseminated FGFR1-amplified ER+ BC cells drives neural/astrocytic interaction, migration and
294 proliferation, resulting in FGFR1-dependent brain colonization. In young hosts, FGFR1 function is
295 mainly driven by astrocytic FGF2, while in aged and E2-depleted mice, neuronal and astrocytic NCAM1
296 serve as non-canonical activators to drive FGFR1 function and ER+ BMs. Consistently, FGFR inhibitors
297 can block early activation and prevent colonization, but not late-stage BCBM which are no longer
298 dependent on this signaling (**Fig. 8m**).

299 **DISCUSSION**

300 FGFR1-amplification has been shown to promote endocrine resistance in ER+ primary BC by
301 maintaining ligand-independent ER transcription[16,17], yet how the TME influences endocrine resistance
302 at metastatic sites is less understood. Here we demonstrate that the increased BM potential of FGFR1+
303 ER+ BC cells results from interactions with canonical and non-canonical FGFR1 activation through
304 astrocytes and neurons during early stages of BM colonization. Moreover, our data demonstrates that
305 TME-mediated activation of FGFR1 in ER+ BCBM is critical for early but not late stages of BM
306 colonization, which has profound implications for the use of FGFR inhibitors clinically. Specifically, our
307 studies provide preclinical rationale for future clinical studies testing FGFR inhibitors in the prevention
308 of BCBM.

309 Our results are in alignment with prior work showing that microenvironment-dependent activation of
310 FGFR1 drives FGFR1-mediated ER signaling and endocrine therapy resistance in primary tumors[14].

311 FGFR ligands secreted by adipose tissue support ER+ primary tumor growth in obese post-
312 menopausal mouse models[20], and cells within the bone TME secrete FGF2 to promote ER+ BC cell
313 plasticity[50]. However, our studies further demonstrate that the levels of FGFR1-activating ligands in the
314 TME are key determinants of the dependency of ER+ BC cells for FGFR1 activation and response to
315 FGFR inhibition. Furthermore, the contact-dependent nature of brain-mediated FGFR1 activation
316 suggests that receptor inhibition or disruption of cell-cell interactions are the most relevant clinical
317 targets for early brain colonization of ER+ BC. While the tumorigenic effect of FGFR1 amplification has
318 been attributed to co-amplified oncogenes in the 8p region[51,52], our FGFR1 KD studies demonstrate its
319 specific role for brain colonization in aged and young hosts. The fact that FGFR1 KD differentially
320 impacted extracranial metastases in aged mice, but not in young/E2 treated mice, further highlights the
321 importance of studying ER+ BC in aged/E2 depleted mice and the context-dependent mechanisms
322 influencing the progression of ER+ metastases.

323 Multiple studies have shown that interactions between disseminated cancer cells and astrocytes can
324 eliminate or support the establishment of brain metastases[53-58]. While these studies have been
325 performed with rapidly growing and aggressive cancer subtypes, our studies are the first to
326 demonstrate brain-specific regulation of ER+ BMs in models that mimic the slow progression of their
327 metastases. Our data showed that young and old astrocytes have different abilities to promote growth
328 of ER+ BC cells, in part through differential expression of FGF2. However, the fact that conditioned
329 media from astrocytes (lacking soluble FGF2) can activate pro-survival signaling in cancer cells in an
330 FGFR1-independent manner, suggests that additional ligands secreted from astrocytes and other cells
331 in the TME are likely to contribute to the progression of ER+ BMs, even those lacking FGFR1
332 amplification. It is possible that these signals from the brain TME contribute to the observed FGFR1-
333 independence of late-stage brain metastases. Further studies are needed to define how additional
334 astrocytic-mediated support of ER BM+ can contribute to late-stage ER+ BCBM progression.

335 Consistent with findings in rats[59,60], our studies show for the first time that E2-suppression and aging
336 downregulate FGF2 levels in the brain niche and directly impact FGFR1 activation. While these
337 differences were initially observed in animals with late-stage BCBM, tumor-naïve mice showed similar

338 FGF2 decreases with age. We showed the novel finding that NCAM1/FGFR1 interactions lead to
339 FGFR1 kinase signaling activation and promote proliferation, invasive and migratory phenotypes in
340 ER+ BC cells. While FGF2 decreases with aging and E2-depletion, NCAM1 expression remained
341 unchanged, suggesting that FGFR1/NCAM interactions contribute to FGFR1 function throughout the
342 progression of ER+ BCBM. Our findings that NCAM1 blockage decrease proliferation of cancer cells in
343 brain slices from old, but not young mice, demonstrate a novel, context dependent mechanism
344 controlling FGFR1 through the lifespan. Since the affinity of FGF for FGFR is approximately 10^6 times
345 higher than that of NCAM1 for FGFR[31,32], higher FGF2 levels drive FGFR1 activation and function in
346 young females. By contrast, NCAM1, which is constantly present cell surfaces at a much higher
347 concentration (micromolar) than FGFs, emerged as an alternative driver in the aged/E2-depleted brain
348 TME[30-32,43,61]. We recognize that our studies cannot fully address the individual contribution of brain
349 FGF2 versus NCAM1 to FGFR1 function in young versus aged females, yet our findings align with
350 studies in HeLa cells showing that despite similar kinase signaling activation, FGF2 and NCAM1 can
351 result in different cellular responses[44,62]. The extent to which FGF2 and NCAM induce differential levels
352 of pFGFR1 or trigger different recycling of FGFR from the cell membrane may explain the slower
353 progression of metastases in older mice and the differential susceptibility of young and aged hosts to
354 kinase inhibitors[44].

355 Seminal studies demonstrated that brain metastatic growth of cancer cells depends on their ability to
356 form synapses with neurons[47,48], similar to findings in glioma cells[63,64]. Additional studies suggest that
357 formation of synaptic structures involving presynaptic neurons, astrocytes, and tumor cells is a critical
358 adaptation for BM colonization[46]. Our data showing that FGFR1 promotes increased synaptic puncta
359 with neurons is suggestive of cancer-neuron synapse formation. While definitive proof that these
360 interactions result in synaptic communication in ER+ BC cells is warranted, the formation of synaptic
361 puncta and the migration of BC cells along neuronal tracks suggest that these cancer-neuron and
362 FGFR1/NCAM1 interactions are implicated in the progression of ER+ BCBM. FGFR1 KD impairing ER+
363 BC cell migration along neurites further supports the notion that NCAM1/FGFR1 interaction is critical for
364 the ability of ER+ BC cells to adhere to neurons and astrocytes, particularly during the early stages of

365 BM colonization. FGFR1 KD UCD65 and UCD12 cells showed decreased brain signal (but not
366 extracranial signal) immediately following intracardiac injection, suggesting that FGFR1 interactions
367 with the brain TME are essential for early colonization or survival of disseminated cells upon arrival to
368 the brain. Consistently, FGFR1 kinase inhibition decreased FGFR1 activation in early disseminated
369 cancer cells and resulted in decreased number of micro metastases in both young and aged hosts,
370 highlighting the potential value for FGFR1 inhibition in the prevention of BMs.

371 Our studies also show that late-stage FGFR1+ ER+ BMs are no longer dependent on FGFR1
372 activation. If this FGFR1-independence in large tumors occurs also in primary tumors or other
373 metastatic sites, there could be an explanation for why FGFR1 amplification does not predict response
374 to this therapy[65]. Further studies are needed to determine whether other FGFR1 inhibitors or increased
375 brain-penetrance of these drugs may be more effective in a therapeutic setting[66]. Collectively, our work
376 demonstrates that changes in the brain TME mediate FGFR1-amplified ER+ BCBM progression
377 through interactions with astrocytes and neurons, which are critical for early brain metastatic
378 colonization but not late progression. Importantly, our studies caution that current strategies to block
379 FGFR1 function are ineffective to block non-canonical functions of FGFR1, particularly in elderly/E2-
380 suppressed patients, and suggest that accounting for host-specific FGFR1 activation may better predict
381 response to FGFR inhibitors than amplification status alone.

382 **MATERIALS AND METHODS**

383 **Ethics Statement:** All animal experiments and procedures were performed in an AAALAC-accredited
384 facility and approved by the University of Colorado Denver | Anschutz Medical Campus Institutional
385 Animal Care and Use Committee and by the DOD Animal Care and Use Review Office. Archival de-
386 identified brain metastasis human samples were obtained under approved IRB protocols at the
387 University of Colorado.

388 **Patient samples:** ER+ BCBM (n = 45), including $ER^+/HER2^-$ (n = 30), $ER^+/HER2^+$ (n = 14), and
389 $ER^+/PR^+/HER2^+$ (n = 1) from archival de-identified human brain metastases samples were obtained
390 under secondary use Colorado Multiple Institutional Review Board (COMIRB) protocol 23-1713 from
391 the University of Colorado tissue biorepository (waiver of consent COMIRB protocol 15-1461).

392 **Cell Lines and Culture:** ER^{Low}-TN UCD46 and ER+ UCD4, UCD12, and UCD65 cell lines[38] were
393 cultured in DMEM/F12 with 10% FBS, P/S, 100ng/mL cholera toxin, and 1nM insulin. MCF7 (FGFR1-
394 OE and EV) were cultured in MEM with EBSS, 10% FBS, P/S, 1x MEM amino acid solution, 1x MEM
395 non-essential amino acids, and 1mM sodium pyruvate. SH-SY5Y cells were purchased from the Cell
396 Technologies Shared Resource (RRID: SCR_021982) and maintained in DMEM/F12 with 10% FBS
397 and P/S. Human astrocytes (Cat. #1800) were purchased from ScienceCell™ Research Laboratories
398 and maintained in astrocyte medium (AM, Cat. #1801) in flasks coated with Poly-L-Lysine (1ug/ml).
399 Estrogen-free variations of all medias were created using phenol red-free media base and 2-5%
400 charcoal-stripped FBS. Starvation media were created using phenol red-free media, no FBS, and 0.1%
401 BSA.

402 ***In vivo* modeling of ER+ BC metastases:** All *in vivo* studies were completed in NOD-*scid* $IL2Rg^{null}$
403 (NSG) mice. Since circulating levels of E2 in gonadal intact young-female mice (2.7± 1 pg/ml) are similar
404 to those of post-menopausal women (1.3-4.9 pg/ml)[10], we mimicked post-menopausal BC using naïve
405 (non-operated) or sham-operated aged females[11]. To study brain metastatic colonization, we use well
406 recognized experimental models of metastasis, where cells are injected intracardially or in the carotid
407 artery to bypass the exit from primary tumor and allow studies of seeding and metastatic colonization in

408 the brain[67-69]. 500,000 cells were injected into the left ventricle of female NSG mice. Intracarotid artery
409 injections were performed as previously described[67]. Spontaneous metastasis models were generated
410 by injecting cells into the mammary fat pad of OVX NSG mice supplemented with E2. Tumors were
411 removed after reaching 1 cm^3, and mice were randomized into indicated groups. Injection success and
412 luciferase-transfected cell growth were tracked via live bioluminescence imaging (BLI) using an IVIS®
413 Spectrum optical scanner following subcutaneous injection of luciferin substrate (D-Luciferin, Potassium
414 Salt, GoldBio 115144-35-9). For spontaneous models, the primary tumor site was covered during BLI
415 measurements. BLI measurements included tumor-free mice to establish background. For mice treated
416 with BGJ398 (Selleck Chemicals S2183), aliquots of drug were prepared daily and delivered via oral
417 gavage of 100μL in 1% CMC. Drug and vehicle were provided 5 times weekly.

418 **Histological Quantification of Brain Metastases:** Intraparenchymal BM were quantified as previously
419 described[57]. Briefly, six hematoxylin and eosin (H&E)–stained sagittal brain sections (20μm thick) were
420 examined per mouse. Sections were collected from the right hemisphere at 300μm intervals and analyzed
421 using an ocular grid with a 4× objective. Micrometastases (defined as lesions measuring ≤300μm along
422 their longest axis), and macrometastases (>300μm) were counted in each section by an investigator
423 blinded to treatment group. Metastatic clusters were defined as groups of one or more micro or
424 macrometastases in close spatial proximity as a readout of likely independent metastatic lesions.
425 Numbers shown are the sum of counts from the six sections.

426 **Magnetic Resonance Imaging (MRI) and Analysis:** To assess metastatic spread non-invasively, mice
427 underwent MRI 16 weeks after tumor cell injection. Brain MRI was performed on anesthetized mice
428 (1.5% isoflurane) using a 9.4 Tesla BioSpec animal MRI scanner (Bruker Medical, Billerica, MA)
429 equipped with a 4-chanel phase-array mouse brain coil at the Colorado Animal Imaging Shared
430 Resource (AISR). Each MRI session consisted of a tri-pilot localizer, followed by a high resolution T2-
431 weighted fast spin echo (T2-turboRARE: field of view = 3 × 3 cm; repetition time = 4000ms; echo time =
432 80ms; slice thickness = 0.7 mm; 256 × 256 matrix size; 4 averages) with a 52-micron in-plane
433 resolution[70,71].

434 Total acquisition time for all sequences was 12 min 21 sec. The total metastatic gross volumes were
435 quantified by placing hand-driven region of interest (ROI) on sequential axial and/ or sagittal T2-
436 turboRARE images, summing total ROI areas and multiplying by 0.7 mm slice thickness (reported in
437 mm3). The largest diameters of larger metastatic lesions were also reported for axial MR images. All
438 MR image acquisition and analysis were performed using Bruker ParaVision 360neo v3.3 software. All
439 image analysis was performed by an MRI physicist with >15 years of experience (NJS).

440 **Immunoblots:** Membranes were blocked with 3% BSA in TBST and probed overnight with antibodies
441 against FGFR1 (Abcam ab76464), pFGFR1 (Y654, Abcam ab59194; Y653/Y654, Cell Signaling
442 52928S), Akt (Cell Signaling 9272S), pAkt (S473, Cell Signaling 4060S), ERK (Cell Signaling 9102S),
443 pERK (T202/T204, Cell Signaling 9101S), and NCAM1 (R&D AF2408), with GAPDH (Cell Signaling
444 97166S) or Tubulin (Sigma T5168) as loading controls. Membranes were washed with TBST and
445 probed with secondary antibodies (Invitrogen A11371, A21109, A21058, A21084, A11374) for 1-2hrs.
446 Blots were imaged on LiCor Odessey CLx and analyzed with ImageStudio Version 5.0 and 6.0. For
447 multiple stains, blots were stripped (Millipore 2504) and reprobed as above.

448 **qRT-PCR:** RNA was isolated with Trizol Reagent (Invitrogen 15596026) and reverse transcribed with
449 Verso cDNA Synthesis Kit (Thermo AB-1453). cDNA was used to perform qPCR with PowerUp SYBR
450 Green Master Mix (Applied Biosystems A25742) on Applied Biosystems QuantStudio 6 Flex. Gene
451 expression was calculated via ddCt. Primer Sequences:

452 *FGFR1* (F: AACCTGACCACAGAATTGGAGGCT, R: TGCTGCCGTACTCATTCTCCACA)

453 *NCAM1* (F: AATTTACCGCGGCAAGAACATC, R: CCTGGCTGGGAACAATATCCAC)

454 *RPLP0* (F: GTGATGTGCAGCTGATCAAGACT, R: GATGACCAGCCCAAAGGAGA)

455 **Primary Astrocyte Culture and Co-culture:** Brains from P0-P1 CD1 mouse pups were dissected, and
456 primary astrocytes were isolated and cultured as previously described[72]. For co-culture experiments,
457 50,000 or 10,000 cancer cells were seeded into 6-well or 24-well plates coated with laminin (1µg/ml),
458 respectively, onto astrocyte monolayers at 100% confluence in E2-free medium (DMEM/F12 phenol
459 red-free, supplemented with 5% charcoal-stripped FBS, 0.1% BSA, 1x penicillin/streptomycin, 1x non-

460 essential amino acids, 1x sodium pyruvate, and 1 nM insulin). Aged mouse astrocytes (aged-mAst)
461 were generated by maintaining cultures in growth medium (DMEM + 10% FBS, 1% P/S) for three
462 months prior to co-culture[73]. In contrast, mAst P0 refers to astrocytes maintained *in vitro* for only 8
463 days. For co-culture with human astrocytes, cells were seeded under the same conditions as murine
464 astrocytes. To generate 10x or 20x concentrated astrocyte-conditioned media (CM), confluent astrocyte
465 cultures were incubated for 72 hours in serum-free, phenol red-free DMEM/F12. Supernatants were
466 then collected and concentrated using 3,000Da molecular weight centrifugal filters.

467 **Isolation of Primary Cells from Adult Mouse Brain:** Whole brain tissue was dissected from young
468 (12 weeks) and aged (>56 weeks) female NSG mice following PBS cardiac perfusion. Cell suspensions
469 were obtained via enzymatic dissociation using the Papain Dissociation System (Worthington
470 Biochemical, LK003150), followed by magnetic-activated cell sorting (MACS; Miltenyi Biotec) according
471 to the manufacturer's instructions. Cell-type-specific isolation was performed using the following
472 reagents from Miltenyi Biotec: Myelin Removal Beads II (130-096-733) for oligodendrocytes, CD11b
473 MicroBeads (130-093-634) for microglia, Anti-ACSA-2 MicroBeads (130-097-678) for astrocytes, and
474 the Neuron Isolation Kit (130-115-389) for neurons.

475 **FGF2 ELISA:** Levels of FGF2 were quantified using the Mouse/Rat FGF basic/FGF2/bFGF Quantikine
476 ELISA Kit (R&D Systems, MFB00) according to the manufacturer's instructions.

477 **Lentivirus and AAV:** The following shRNA plasmids were purchased from the Functional Genomics
478 Shared Resources (RRID:SCR_021987): TRCN0000121186, TRCN0000000419, and
479 TRCN0000000418 targeting human FGFR1; TRCN0000373085 and TRCN0000373034 targeting
480 NCAM1, TRCN0000355839 targeting Fgf2. MISSION® shRNA Plasmid DNA Control Vectors SHC216
481 and SCH002 were purchased from Sigma. Lentiviral particles were produced in 293-T cells and
482 concentrated via ultracentrifugation. Viral particles were added to all cells with 6μg/mL polybrene and
483 cancer cells were selected with 2μg/mL puromycin. For transduction of astrocytes, lentivirus was not
484 concentrated and cells were not selected. AAV shRNA particles were purchased from PackGene and
485 designed to include CMV-mCherry as a reporter and the same shRNA sequences as

486 TRCN0000355839 (Fgf2) and TRCN0000373085 (Ncam1). Control AAV was purchased from
487 AAVnerGene (DP001006). Astrocytes were infected with 10,000 viral particles per cell.

488 **Organotypic Co-culture:** GFP+ cancer cells were cultured in ultra-low attachment plates to form
489 spheroids. NSG mice were sacrificed and brains excised, sectioned into 250μm coronal slices, and
490 collected in 1x HBSS with 2.5mM HEPES, 30mM D-Glucose, 1mM CaCl2, 1mM MgSO4, and 4mM
491 NaHCO3 (Complete HBSS). Slices were plated in 12-well transwells. 1mL of media containing 25%
492 complete HBSS, 25% donor equine serum, 50% MEM, 1x GlutaMAX (Gibco 35050061), and P/S was
493 added to the well below the transwell. Spheroids of cancer cells were plated on top of the brain slices in
494 <2μL media. Spheres were allowed to settle for 24 hours and images were acquired via stereo
495 fluorescent microscopy every 48 hours. Growth was quantified via GFP intensity corrected for
496 background autofluorescence of adjacent brain tissue (ImageJ). For treatments of organotypic brain
497 slices with IgG (Sigma M5284), αFGF2 (Antibody System RMC38201), or αNCAM1(Sigma AB5032)
498 neutralizing antibodies, 0.5μg was added on top of each slice in 10μL, with an additional 0.5μg added
499 to the media in the well below. Spheroids of UCD12 cells were plated 24 hours after antibody treatment.

500 **Immunohistochemistry and Immunofluorescence:** Formalin-fixed, paraffin-embedded sections of
501 ER^+ BCBM from patient samples obtained at the University of Colorado were deparaffinized in xylene
502 and rehydrated through a graded ethanol series to distilled water. Heat-induced antigen retrieval was
503 performed in 10 mM citrate buffer (pH 6.0) or Tris-EDTA buffer (pH 9.0) at 125 °C and 25 psi for 10
504 minutes. Endogenous peroxidase activity was quenched with 3% hydrogen peroxide, and sections
505 were blocked with 10% normal horse serum (ImmPRESS, Vector Laboratories). Slides were incubated
506 overnight at RT with primary antibodies against FGFR1 (Invitrogen PA5-25979) or pFGFR1 (Y654,
507 Abcam ab59194), followed by HRP-conjugated anti-rabbit IgG (ImmPRESS, Vector Laboratories).
508 Signal was developed using 3,3′-diaminobenzidine (DAB; DAKO). Slides were scanned using an Aperio
509 ScanScope T3 (Leica Biosystems), and membrane expression of FGFR1 and pFGFR1 in tumor cells
510 was quantified using the Aperio Image Analysis software.

511 For immunofluorescence, cells grown on coverslips and free-floating brain slices were fixed with 4%
512 paraformaldehyde (PFA) and heat-induced antigen retrieval was performed in boiling 10 mM citrate
513 buffer (pH 6.0). Coverslips, slices, or deparaffinized formalin-fixed, paraffin-embedded sections (as
514 described above), were blocked with 10% normal donkey serum (NDS) in TBST for 1 hour at RT.
515 Primary antibodies against GFAP (Invitrogen 12-0300), FGF2 (Novusbio NBP3-15367), pFGFR1
516 (Y654, Abcam ab59194), NCAM1 (R&D AF2408), PanCK (DAKO M0821), Synapsin1/2 (Synaptic
517 Systems 106004), and PSD95 (Invitrogen MA1-045) were incubated for 2 hours or overnight at RT. For
518 double staining, primary antibodies were applied either sequentially in separate incubations or pooled.
519 After washing with PBS containing 0.01% Triton X-100, coverslips, slices, or slides were incubated with
520 secondary antibodies (Jackson ImmunoResearch 712-545-153, 712-585-153, 706-165-148, 715-545-
521 150, 715-585-150, 715-605-150, 705-585-147, 711-545-152, 711-585-152, 711-605-152) diluted in
522 TBST for 2 hours at RT in the dark. Nuclei were stained with DAPI (1 µg/mL in methanol or PBS) for 10
523 minutes at RT and samples were mounted with FluoroMount-G (Southern Biotech).

524 **Growth Assays:** Cells were maintained in E2-free media for 48 hours before being trypsinized with
525 phenol red-free trypsin and plated at densities of 2,000 MCF7, 10,000 UCD12, and 20,000 UCD65 cells
526 per well of duplicate 96-well plates in 100µL of media. Following 24 hours, 100µL of media containing
527 each treatment (2x) was added to the wells of one plate. The duplicate plate was fixed with 10% TCA.
528 Growth was tracked via Incucyte S3 system where 10x phase contrast and GFP images were obtained
529 every 12 hours. Treatments were maintained by regularly changing 50% of media. At the conclusion of
530 the Incucyte tracking, plates were fixed with 10% TCA. Fixed plates were stained with 0.04% SRB
531 (Sigma) and total protein was quantified via plate reader measurements at 565, 525, and 490nm
532 subtracting 690nm background. Proliferation was additionally measured by quantifying fold change of
533 SRB signal between the two plates.

534 **Digital Spatial Transcriptomics:** Female NSG mice were ovariectomized or sham operated and 15
535 days later injected via intracarotid artery with 250,000 UCD65 GFPLuc+ cells. Mice were classified
536 according to their age as young (between 7 and 15 weeks) or aged (>60 weeks). Development of brain
537 metastasis was monitored during 15 weeks via IVIS. Six months after injection, animals were

538 euthanized by ketamine/xylazine overdose and perfused with PBS/4%PFA. Brains were cryopreserved
539 in 20% sucrose and stored at 4°C. Paraffin embedded fixed coronal sections were stained with
540 antibodies targeting PanCK (DAKO M0821), Iba1 (WAKO PTG5394), GFAP (Invitrogen 13-0300) and
541 DAPI. One set of brain sections from young-sham, aged-sham, young-OVX and aged-OVX mice (n = 1
542 animal per condition) were probed by in situ hybridization with the GeoMx® Mouse Whole
543 Transcriptome Atlas (WTA) library. Then, using the GeoMX Digital Spatial Profiler (DSP), barcoded
544 RNA-probes in the Iba+/GFAP+ regions of interest (ROI) within a maximum of 400µm from PanCK+
545 BCBM were UV-cleaved and processed by Illumina sequencing. Similarly, another set of brain sections
546 from young-sham and aged-sham mice were probed by in situ hybridization with the GeoMx® Human
547 WTA library. Then, with the GeoMX DSP, RNA-probes in the PanCK+ ROIs (human breast cancer cells)
548 were UV-cleaved and processed by Illumina sequencing. A total of 48 Iba+/GFAP+ ROIs (young-sham
549 = 18, aged-sham = 16, young-OVX = 9, and aged-OVX = 5) and 59 PanCK+ ROIs (aged-sham = 16
550 and young-sham = 43) were retrieved and sequenced using an Illumina NovaSeq X plus sequencer in
551 one lane on a 10B flow cell at 2x150bp configuration. Sequencing was performed by the Genomics
552 Shared Resource (RRID: SCR_021984).

553 Using the GeoMx® NGS Pipeline (Nanostring) and the Probe Kit Configuration (PKC) files for Human
554 or Mouse RNA WTA, the FASTQ libraries were processed to obtain the Digital Count Conversion (DCC)
555 files. DCC files were analyzed in R (4.4.2) with NanoStringNCTools[74], GeomxTools[75] and
556 GeoMxWorkflows[76] packages. All ROIs with gene detection rate (defined as the number of genes in the
557 sample divided by the number of genes in the WTA) above 1%, more than 100 nuclei, and all probes in
558 the highest quartile above the background reading were retained for further analysis (**Supplementary**
559 **Fig. 3**). Raw counts were normalized using the Q3 method in NanoStringNCTools. Normalized counts
560 were used to UMAP analysis with the umap package in R. Differential expression analyses were
561 performed with limma-voom in standR[77,78] using the GeoMXAnalysisWorkflow package in R[79].
562 Differentially expressed genes were visualized as MA plots with ggplot2.

563 Log-CPM (counts per million) values were transformed with “voom” to get the appropriate observation-
564 level weights and fitted to a linear model with “fit”. Then using “contrasts.fit”, the array was used to get

565 estimated coefficients and standard errors for each pairwise comparison. Finally, the differential
566 expression statistics were computed using empirical Bayes moderation with “ebayes”. Differentially
567 expressed genes lists were used to perform a gene sets enrichment analysis (GSEA) following the
568 GeoMXAnalysisWorkflow method[79]. Briefly, MSigDB Hallmarks, MSigDB C2, Gene Ontology and
569 KEGG databases were downloaded in R using the msigdb and GSEABase libraries[80,81]. Enrichment
570 analyses were performed using fry from the limma package[78]. Finally, using vissE package[82] we
571 clustered significant (FDR <0.05) enriched gene sets based on the genes overlap with a threshold of
572 35%. Clusters were further analyzed by text mining to identify common biological patterns using the
573 gene set names. Additionally, frequency of each gene in each cluster was plotted vs their respective
574 log_2FC. Clusters were ranked by size and FDR and top 9 clusters were plotted using igraph[83].

575 **Recombinant protein treatment for downstream signaling**: 1 million UCD65, UCD12, or MCF7 cells
576 were plated in 60mm plates. 12 hours after plating, cells were washed three times with PBS and media
577 was replaced with starvation media. Following 48-72 hours in starvation media, media was replaced
578 with starvation media containing the indicated concentrations of FGF2 (PeproTech AF-100-18B) or
579 NCAM1 (Acro Biosystems NC1-H5223). Pretreatments with BGJ398 (Selleck Chemicals S2183) were
580 completed 1 hour prior to treatments. Following treatment, protein was collected in RIPA buffer.

581 **RNA Sequencing**: UCD65 and UCD12 cells were serum-starved and then treated with vehicle,
582 10ng/mL FGF2, or 20ug/mL for 24hr. RNA was isolated with Trizol Reagent (Invitrogen 15596026)
583 followed by RNeasy Cleanup Kit (Qiagen 74204). mRNA libraries were created using poly-A enrichment
584 and sequenced at 40M PE150 reads by NovaSeq X Plus Series (Illumina). Reads were filtered by
585 quality (removal of reads containing adaptors, >10% undetermined bases, and QScore <5 for 50% of
586 bases) and aligned with HiSAT2 (2.2.1) to Homo Sapiens Reference Genome (GRCh38/hg38). Raw
587 counts were obtained with featureCounts (2.0.6), and analyzed in R 4.5.0. Normalized counts and
588 differential expression were obtained with deseq2[84] and used to perform gene sets enrichment analysis
589 (GSEA) as described above for digital spatial transcriptomics, clustered based on 25% gene overlap.

590 **Primary Neuron Culture and Co-Culture:** Hippocampi were dissected from P0-1 CD1 pups and
591 neurons were isolated as previously described[85]. Primary neurons were cultured on poly-l-lysine coated
592 coverslips in 24-well plates and maintained in phenol red-free neurobasal media supplemented with
593 GlutaMAX, 1x B27, and P/S, with 50% media replaced twice weekly. Five days after isolation, 1.5μM
594 cytosine arabinoside was added to each well. After 48 hours, 50% media was replaced. For co-cultures,
595 5,000-10,000 cancer cells were added to each well 24 hours after cytosine arabinoside removal. Co-
596 cultures grew for 5-10 additional days before coverslips were fixed.

597 **Synapse Detection and Quantification:** Synapsin1/2 and PSD95 were costained via
598 immunofluorescence and samples were imaged via confocal microscopy (3I MARIANAS Inverted
599 Spinning Disk) at 40x magnification. SynQuant ImageJ plugin[86] was used to quantify synapses as
600 punctate co-localization of the two markers, and synapse number was controlled for analysis area
601 differences between images.

602 **Neural Migration Analysis:** Phase and GFP images were collected every 12 hours. GFP+ ROIs were
603 defined to indicate cells in each image. Using ImageJ, phase images were used to stabilize motion
604 across time points[87], and these corrections were applied to the GFP+ ROIs. Movement was tracked
605 using TrackMate[88,89].

606 **Statistical Analysis and Reproducibility:** Statistical analyses are specified in figure legends and were
607 performed with GraphPad Prism 10.4.2 for predetermined comparisons only. All tests were 2-tailed.
608 Statistical analysis of sequencing data was performed in R 4.4.2 and 4.5.0. For animal experiments
609 involving injections of different cells, groups were littermate-matched and injections were blinded. For
610 treatment of established tumors, groups were randomized. In studies involving aged mice, there was
611 expected age-related, non-tumor related mortality. These animals were excluded from final analysis
612 and initial group sizes were 20% larger to account for this loss. Where possible, analyses were blinded
613 to experimental conditions or performed using automated functions to reduce bias.

614 **Data Availability:** Digital Spatial Profiling and RNA-sequencing data will be uploaded to NCBI's Gene
615 Expression Omnibus prior to publication.

616 **Code Availability:** All information is provided in the Methods, including packages, software, and
617 pipelines. No custom code was generated during these studies. Source Data are provided with this
618 paper.

619 **REFERENCES**

620 1 Kaal, E. C. A., Niël, C. G. J. H. & Vecht, C. J. Therapeutic management of brain metastasis. *The*
621 *Lancet Neurology* **4**, 289-298 (2005). https://doi.org/10.1016/S1474-4422(05)70072-7
622 2 Palmieri, D. *et al.* Brain metastases of breast cancer. *Breast disease* **26**, 139-147 (2006).
623 3 Morris, P. G. *et al.* Limited Overall Survival in Patients with Brain Metastases from Triple
624 Negative Breast Cancer. *The Breast Journal* **18**, 345-350 (2012). https://doi.org/10.1111/j.1524-
625 4741.2012.01246.x
626 4 Press, D. J., Miller, M. E., Liederbach, E., Yao, K. & Huo, D. De novo metastasis in breast
627 cancer: occurrence and overall survival stratified by molecular subtype. *Clin Exp Metastasis* **34**,
628 457-465 (2017). https://doi.org/10.1007/s10585-017-9871-9
629 5 Kennecke, H. *et al.* Metastatic behavior of breast cancer subtypes. *J Clin Oncol* **28**, 3271-3277
630 (2010). https://doi.org/10.1200/JCO.2009.25.9820
631 6 Heitz, F. *et al.* Triple-negative and HER2-overexpressing breast cancers exhibit an elevated risk
632 and an earlier occurrence of cerebral metastases. *Eur J Cancer* **45**, 2792-2798 (2009).
633 https://doi.org/10.1016/j.ejca.2009.06.027
634 7 Chatzistamou, I. & Kiaris, H. Modeling estrogen receptor-positive breast cancers in mice: is it
635 the best we can do? *Endocr Relat Cancer* **23**, C9-C12 (2016). https://doi.org/10.1530/ERC-16-
636 0397
637 8 Sledge, G. W. *et al.* Past, present, and future challenges in breast cancer treatment. *J Clin*
638 *Oncol* **32**, 1979-1986 (2014). https://doi.org/10.1200/JCO.2014.55.4139
639 9 Turrell, F. K. *et al.* Age-associated microenvironmental changes highlight the role of PDGF-C in
640 ER(+) breast cancer metastatic relapse. *Nat Cancer* **4**, 468-484 (2023).
641 https://doi.org/10.1038/s43018-023-00525-y
642 10 Rothman, M. S. *et al.* Reexamination of testosterone, dihydrotestosterone, estradiol and estrone
643 levels across the menstrual cycle and in postmenopausal women measured by liquid
644 chromatography-tandem mass spectrometry. *Steroids* **76**, 177-182 (2011).
645 https://doi.org/10.1016/j.steroids.2010.10.010

646 11 Osborne, C. K., Hobbs, K. & Clark, G. M. Effect of estrogens and antiestrogens on growth of
647 human breast cancer cells in athymic nude mice. *Cancer Res* **45**, 584-590 (1985).
648 12 Offner, H. & Polanczyk, M. A potential role for estrogen in experimental autoimmune
649 encephalomyelitis and multiple sclerosis. *Ann N Y Acad Sci* **1089**, 343-372 (2006).
650 https://doi.org/10.1196/annals.1386.021
651 13 Guerini-Rocco, E. *et al.* Genomic Aberrations and Late Recurrence in Postmenopausal Women
652 with Hormone Receptor-positive Early Breast Cancer: Results from the SOLE Trial. *Clin Cancer*
653 *Res* (2021). https://doi.org/10.1158/1078-0432.CCR-20-0126
654 14 DiGiacomo, J. W., Godet, I., Trautmann-Rodriguez, M. & Gilkes, D. M. Extracellular Matrix-
655 Bound FGF2 Mediates Estrogen Receptor Signaling and Therapeutic Response in Breast
656 Cancer. *Mol Cancer Res* **19**, 136-149 (2021). https://doi.org/10.1158/1541-7786.MCR-20-0554
657 15 Garcia-Recio, S. *et al.* FGFR4 regulates tumor subtype differentiation in luminal breast cancer
658 and metastatic disease. *J Clin Invest* **130**, 4871-4887 (2020). https://doi.org/10.1172/JCI130323
659 16 Formisano, L. *et al.* Aberrant FGFR signaling mediates resistance to CDK4/6 inhibitors in ER+
660 breast cancer. *Nat Commun* **10**, 1373 (2019). https://doi.org/10.1038/s41467-019-09068-2
661 17 Drago, J. Z. *et al.* FGFR1 Amplification Mediates Endocrine Resistance but Retains TORC
662 Sensitivity in Metastatic Hormone Receptor-Positive (HR(+)) Breast Cancer. *Clin Cancer Res*
663 **25**, 6443-6451 (2019). https://doi.org/10.1158/1078-0432.CCR-19-0138
664 18 Ding, K. *et al.* FGFR4 in endocrine resistance: overexpression and estrogen regulation without
665 direct causative role. *Breast Cancer Res Treat* **211**, 501-515 (2025).
666 https://doi.org/10.1007/s10549-025-07666-x
667 19 Xie, N. *et al.* FGFR aberrations increase the risk of brain metastases and predict poor prognosis
668 in metastatic breast cancer patients. *Ther Adv Med Oncol* **12**, 1758835920915305 (2020).
669 https://doi.org/10.1177/1758835920915305
670 20 Wellberg, E. A. *et al.* FGFR1 underlies obesity-associated progression of estrogen receptor-
671 positive breast cancer after estrogen deprivation. *JCI Insight* **3** (2018).
672 https://doi.org/10.1172/jci.insight.120594

673 21 Sytnyk, V., Leshchyns'ka, I. & Schachner, M. Neural Cell Adhesion Molecules of the
674 Immunoglobulin Superfamily Regulate Synapse Formation, Maintenance, and Function. *Trends*
675 *Neurosci* **40**, 295-308 (2017). https://doi.org/10.1016/j.tins.2017.03.003
676 22 Dabrowski, A., Terauchi, A., Strong, C. & Umemori, H. Distinct sets of FGF receptors sculpt
677 excitatory and inhibitory synaptogenesis. *Development* **142**, 1818-1830 (2015).
678 https://doi.org/10.1242/dev.115568
679 23 Terauchi, A. *et al.* Distinct FGFs promote differentiation of excitatory and inhibitory synapses.
680 *Nature* **465**, 783-787 (2010). https://doi.org/10.1038/nature09041
681 24 Umemori, H., Linhoff, M. W., Ornitz, D. M. & Sanes, J. R. FGF22 and its close relatives are
682 presynaptic organizing molecules in the mammalian brain. *Cell* **118**, 257-270 (2004).
683 https://doi.org/10.1016/j.cell.2004.06.025
684 25 Klimaschewski, L. & Claus, P. Fibroblast Growth Factor Signalling in the Diseased Nervous
685 System. *Mol Neurobiol* **58**, 3884-3902 (2021). https://doi.org/10.1007/s12035-021-02367-0
686 26 Ohkubo, Y., Uchida, A. O., Shin, D., Partanen, J. & Vaccarino, F. M. Fibroblast growth factor
687 receptor 1 is required for the proliferation of hippocampal progenitor cells and for hippocampal
688 growth in mouse. *J Neurosci* **24**, 6057-6069 (2004). https://doi.org/10.1523/JNEUROSCI.1140-
689 04.2004
690 27 Gonzalez, A. M., Berry, M., Maher, P. A., Logan, A. & Baird, A. A comprehensive analysis of the
691 distribution of FGF-2 and FGFR1 in the rat brain. *Brain Res* **701**, 201-226 (1995).
692 https://doi.org/10.1016/0006-8993(95)01002-x
693 28 Ma, D. K., Ponnusamy, K., Song, M. R., Ming, G. L. & Song, H. Molecular genetic analysis of
694 FGFR1 signalling reveals distinct roles of MAPK and PLCgamma1 activation for self-renewal of
695 adult neural stem cells. *Mol Brain* **2**, 16 (2009). https://doi.org/10.1186/1756-6606-2-16
696 29 Cambon, K. *et al.* A synthetic neural cell adhesion molecule mimetic peptide promotes
697 synaptogenesis, enhances presynaptic function, and facilitates memory consolidation. *J*
698 *Neurosci* **24**, 4197-4204 (2004). https://doi.org/10.1523/JNEUROSCI.0436-04.2004

699 30 Christensen, C., Berezin, V. & Bock, E. Neural cell adhesion molecule differentially interacts with
700 isoforms of the fibroblast growth factor receptor. *Neuroreport* **22**, 727-732 (2011).
701 https://doi.org/10.1097/WNR.0b013e3283491682
702 31 Kiselyov, V. V., Soroka, V., Berezin, V. & Bock, E. Structural biology of NCAM homophilic binding
703 and activation of FGFR. *J Neurochem* **94**, 1169-1179 (2005). https://doi.org/10.1111/j.1471-
704 4159.2005.03284.x
705 32 Kiselyov, V. V. *et al.* Structural basis for a direct interaction between FGFR1 and NCAM and
706 evidence for a regulatory role of ATP. *Structure* **11**, 691-701 (2003).
707 https://doi.org/10.1016/s0969-2126(03)00096-0
708 33 Krushel, L. A., Tai, M. H., Cunningham, B. A., Edelman, G. M. & Crossin, K. L. Neural cell
709 adhesion molecule (N-CAM) domains and intracellular signaling pathways involved in the
710 inhibition of astrocyte proliferation. *Proc Natl Acad Sci U S A* **95**, 2592-2596 (1998).
711 https://doi.org/10.1073/pnas.95.5.2592
712 34 Kobayashi, S., Vidal, I., Pena, J. D. & Hernandez, M. R. Expression of neural cell adhesion
713 molecule (NCAM) characterizes a subpopulation of type 1 astrocytes in human optic nerve
714 head. *Glia* **20**, 262-273 (1997). https://doi.org/10.1002/(sici)1098-1136(199707)20:3<262::aid-
715 glia10>3.0.co;2-s
716 35 Weledji, E. P. & Assob, J. C. The ubiquitous neural cell adhesion molecule (N-CAM). *Ann Med*
717 *Surg (Lond)* **3**, 77-81 (2014). https://doi.org/10.1016/j.amsu.2014.06.014
718 36 Knafo, S. *et al.* Facilitation of AMPA receptor synaptic delivery as a molecular mechanism for
719 cognitive enhancement. *PLoS Biol* **10**, e1001262 (2012).
720 https://doi.org/10.1371/journal.pbio.1001262
721 37 Leshchyns'ka, I., Sytnyk, V., Morrow, J. S. & Schachner, M. Neural cell adhesion molecule
722 (NCAM) association with PKCbeta2 via betaI spectrin is implicated in NCAM-mediated neurite
723 outgrowth. *J Cell Biol* **161**, 625-639 (2003). https://doi.org/10.1083/jcb.200303020
724 38 Finlay-Schultz, J. *et al.* New generation breast cancer cell lines developed from patient-derived
725 xenografts. *Breast Cancer Res* **22**, 68 (2020). https://doi.org/10.1186/s13058-020-01300-y

726 39 Finlay-Schultz, J. *et al.* Breast Cancer Suppression by Progesterone Receptors Is Mediated by
727 Their Modulation of Estrogen Receptors and RNA Polymerase III. *Cancer Res* **77**, 4934-4946
728 (2017). https://doi.org/10.1158/0008-5472.CAN-16-3541
729 40 Beenken, A. & Mohammadi, M. The FGF family: biology, pathophysiology and therapy. *Nat Rev*
730 *Drug Discov* **8**, 235-253 (2009). https://doi.org/10.1038/nrd2792
731 41 Plotnikov, A. N., Schlessinger, J., Hubbard, S. R. & Mohammadi, M. Structural basis for FGF
732 receptor dimerization and activation. *Cell* **98**, 641-650 (1999). https://doi.org/10.1016/s0092-
733 8674(00)80051-3
734 42 Schlessinger, J. *et al.* Crystal structure of a ternary FGF-FGFR-heparin complex reveals a dual
735 role for heparin in FGFR binding and dimerization. *Mol Cell* **6**, 743-750 (2000).
736 https://doi.org/10.1016/s1097-2765(00)00073-3
737 43 Aonurm-Helm, A., Berezin, V., Bock, E. & Zharkovsky, A. NCAM-mimetic, FGL peptide, restores
738 disrupted fibroblast growth factor receptor (FGFR) phosphorylation and FGFR mediated
739 signaling in neural cell adhesion molecule (NCAM)-deficient mice. *Brain Res* **1309**, 1-8 (2010).
740 https://doi.org/10.1016/j.brainres.2009.11.003
741 44 Francavilla, C. *et al.* The binding of NCAM to FGFR1 induces a specific cellular response
742 mediated by receptor trafficking. *J Cell Biol* **187**, 1101-1116 (2009).
743 https://doi.org/10.1083/jcb.200903030
744 45 Niethammer, P. *et al.* Cosignaling of NCAM via lipid rafts and the FGF receptor is required for
745 neuritogenesis. *J Cell Biol* **157**, 521-532 (2002). https://doi.org/10.1083/jcb.200109059
746 46 Zeng, Q. *et al.* Synaptic proximity enables NMDAR signalling to promote brain metastasis.
747 *Nature* **573**, 526-531 (2019). https://doi.org/10.1038/s41586-019-1576-6
748 47 Venkataramani, V. *et al.* Direct excitatory synapses between neurons and tumor cells drive brain
749 metastatic seeding of breast cancer and melanoma. *bioRxiv*, 2024.2001.2008.574608 (2024).
750 https://doi.org/10.1101/2024.01.08.574608
751 48 Savchuk, S. *et al.* Neuronal activity-dependent mechanisms of small cell lung cancer
752 pathogenesis. *Nature* **646**, 1232-1242 (2025). https://doi.org/10.1038/s41586-025-09492-z

753 49 Lassman, A. B. *et al.* Infigratinib in Patients with Recurrent Gliomas and FGFR Alterations: A
754 Multicenter Phase II Study. *Clin Cancer Res* **28**, 2270-2277 (2022).
755 https://doi.org/10.1158/1078-0432.CCR-21-2664
756 50 Bado, I. L. *et al.* The bone microenvironment increases phenotypic plasticity of ER(+) breast
757 cancer cells. *Dev Cell* **56**, 1100-1117 e1109 (2021). https://doi.org/10.1016/j.devcel.2021.03.008
758 51 Ray, M. E. *et al.* Genomic and expression analysis of the 8p11-12 amplicon in human breast
759 cancer cell lines. *Cancer Res* **64**, 40-47 (2004). https://doi.org/10.1158/0008-5472.can-03-1022
760 52 Voutsadakis, I. A. 8p11.23 Amplification in Breast Cancer: Molecular Characteristics, Prognosis
761 and Targeted Therapy. *J Clin Med* **9** (2020). https://doi.org/10.3390/jcm9103079
762 53 Chen, Q. *et al.* Carcinoma-astrocyte gap junctions promote brain metastasis by cGAMP
763 transfer. *Nature* **533**, 493-498 (2016). https://doi.org/10.1038/nature18268
764 54 Zhang, L. *et al.* Microenvironment-induced PTEN loss by exosomal microRNA primes brain
765 metastasis outgrowth. *Nature* **527**, 100-104 (2015). https://doi.org/10.1038/nature15376
766 55 Valiente, M. *et al.* Serpins promote cancer cell survival and vascular co-option in brain
767 metastasis. *Cell* **156**, 1002-1016 (2014). https://doi.org/10.1016/j.cell.2014.01.040
768 56 Kienast, Y. *et al.* Real-time imaging reveals the single steps of brain metastasis formation. *Nat*
769 *Med* **16**, 116-122 (2010). https://doi.org/10.1038/nm.2072
770 57 Sartorius, C. A. *et al.* Estrogen promotes the brain metastatic colonization of triple negative
771 breast cancer cells via an astrocyte-mediated paracrine mechanism. *Oncogene* **35**, 2881-2892
772 (2016). https://doi.org/10.1038/onc.2015.353
773 58 Contreras-Zarate, M. J. *et al.* Estradiol induces BDNF/TrkB signaling in triple-negative breast
774 cancer to promote brain metastases. *Oncogene* **38**, 4685-4699 (2019).
775 https://doi.org/10.1038/s41388-019-0756-z
776 59 Chadashvili, T. & Peterson, D. A. Cytoarchitecture of fibroblast growth factor receptor 2 (FGFR-
777 2) immunoreactivity in astrocytes of neurogenic and non-neurogenic regions of the young adult
778 and aged rat brain. *J Comp Neurol* **498**, 1-15 (2006). https://doi.org/10.1002/cne.21009

779 60 Huang, C., Yuan, P., Wu, J. & Huang, J. Estrogen regulates excitatory amino acid carrier 1
780 (EAAC1) expression through sphingosine kinase 1 (SphK1) transacting FGFR-mediated ERK
781 signaling in rat C6 astroglial cells. *Neuroscience* **319**, 9-22 (2016).
782 https://doi.org/10.1016/j.neuroscience.2016.01.027
783 61 Jurgenson, M., Aonurm-Helm, A. & Zharkovsky, A. Partial reduction in neural cell adhesion
784 molecule (NCAM) in heterozygous mice induces depression-related behaviour without cognitive
785 impairment. *Brain Res* **1447**, 106-118 (2012). https://doi.org/10.1016/j.brainres.2012.01.056
786 62 Francavilla, C. *et al.* Neural cell adhesion molecule regulates the cellular response to fibroblast
787 growth factor. *J Cell Sci* **120**, 4388-4394 (2007). https://doi.org/10.1242/jcs.010744
788 63 Venkatesh, H. S. *et al.* Electrical and synaptic integration of glioma into neural circuits. *Nature*
789 **573**, 539-545 (2019). https://doi.org/10.1038/s41586-019-1563-y
790 64 Venkataramani, V. *et al.* Glutamatergic synaptic input to glioma cells drives brain tumour
791 progression. *Nature* **573**, 532-538 (2019). https://doi.org/10.1038/s41586-019-1564-x
792 65 Coombes, R. C. *et al.* Results of the phase IIa RADICAL trial of the FGFR inhibitor AZD4547 in
793 endocrine resistant breast cancer. *Nat Commun* **13**, 3246 (2022).
794 https://doi.org/10.1038/s41467-022-30666-0
795 66 Knight, W. *et al.* Abstract 6296: Preclinical evaluation of a panel of FGFR inhibitors for their
796 normal brain and brain tumor distribution. *Cancer Research* **82**, 6296-6296 (2022).
797 https://doi.org/10.1158/1538-7445.Am2022-6296
798 67 Zhang, C., Lowery, F. J. & Yu, D. Intracarotid Cancer Cell Injection to Produce Mouse Models of
799 Brain Metastasis. *J Vis Exp* (2017). https://doi.org/10.3791/55085
800 68 Zhang, C. & Yu, D. Microenvironment determinants of brain metastasis. *Cell Biosci* **1**, 8 (2011).
801 https://doi.org/10.1186/2045-3701-1-8
802 69 Miarka, L. & Valiente, M. Animal models of brain metastasis. *Neurooncol Adv* **3**, v144-v156
803 (2021). https://doi.org/10.1093/noajnl/vdab115

70 Koza, L. A. *et al.* Immunocal(R) limits gliosis in mouse models of repetitive mild-moderate traumatic brain injury. *Brain Res* **1808**, 148338 (2023). https://doi.org/10.1016/j.brainres.2023.148338

71 Pierce, A. M. *et al.* Establishment of patient-derived orthotopic xenograft model of 1q+ posterior fossa group A ependymoma. *Neuro Oncol* **21**, 1540-1551 (2019). https://doi.org/10.1093/neuonc/noz116

72 de Vellis, J. & Cole, R. Preparation of mixed glial cultures from postnatal rat brain. *Methods Mol Biol* **814**, 49-59 (2012). https://doi.org/10.1007/978-1-61779-452-0_4

73 Pertusa, M., Garcia-Matas, S., Rodriguez-Farre, E., Sanfeliu, C. & Cristofol, R. Astrocytes aged in vitro show a decreased neuroprotective capacity. *J Neurochem* **101**, 794-805 (2007). https://doi.org/10.1111/j.1471-4159.2006.04369.x

74 NanoStringNCTools: NanoString nCounter Tools (2024).

75 GeomxTools: NanoString GeoMx Tools (2024).

76 GeoMxWorkflows: GeoMx Digital Spatial Profiler (DSP) data analysis workflows (2024).

77 Liu, N. *et al.* standR: spatial transcriptomic analysis for GeoMx DSP data. *Nucleic Acids Res* **52**, e2 (2024). https://doi.org/10.1093/nar/gkad1026

78 Ritchie, M. E. *et al.* limma powers differential expression analyses for RNA-sequencing and microarray studies. *Nucleic Acids Res* **43**, e47 (2015). https://doi.org/10.1093/nar/gkv007

79 GeoMXAnalysisWorkflow: GeoMXAnalysisWorkflow (2023).

80 msigdb: An ExperimentHub Package for the Molecular Signatures Database (MSigDB) (2024).

81 GSEABase: Gene set enrichment data structures and methods (2024).

82 vissE: Visualising Set Enrichment Analysis Results (2024).

83 igraph: Network Analysis and Visualization in R (2025).

84 Love, M. I., Huber, W. & Anders, S. Moderated estimation of fold change and dispersion for RNA-seq data with DESeq2. *Genome Biol* **15**, 550 (2014). https://doi.org/10.1186/s13059-014-0550-8

85 Beaudoin, G. M., 3rd *et al.* Culturing pyramidal neurons from the early postnatal mouse hippocampus and cortex. *Nat Protoc* **7**, 1741-1754 (2012). https://doi.org/10.1038/nprot.2012.099

86 Wang, Y. *et al.* SynQuant: an automatic tool to quantify synapses from microscopy images. *Bioinformatics* **36**, 1599-1606 (2020). https://doi.org/10.1093/bioinformatics/btz760

87 "The image stabilizer plugin for ImageJ," https://www.cs.cmu.edu/~kangli/code/Image_Stabilizer.html (2008).

88 Tinevez, J. Y. *et al.* TrackMate: An open and extensible platform for single-particle tracking. *Methods* **115**, 80-90 (2017). https://doi.org/10.1016/j.ymeth.2016.09.016

89 Ershov, D. *et al.* TrackMate 7: integrating state-of-the-art segmentation algorithms into tracking pipelines. *Nat Methods* **19**, 829-832 (2022). https://doi.org/10.1038/s41592-022-01507-1

841 **Acknowledgements/Grant Support:** This study was supported by DoD-BCRP W81XWH-22-1-0042
842 (DMC), R37CA227984 (DMC), T32CA190216 (MSF), F31CA294726 (MSF), University of Colorado
843 Cancer Center Pilot Funds (DMC, CAS), the University of Colorado Cancer Center Support Grant
844 (P30CA046934), and NIH High-End and SIFAR S10 Shared Instrumentation Grants (S10OD023485 and
845 S10OD027023). PK is supported by R01CA258766. We would like to thank the Biorepository Core
846 Facility and personnel at the CU Brain Tumor Biorepository for providing de-identified human tissues,
847 Animal Imaging Shared Resource and Jenna Steiner, Genomics Shared Resource and Schuyler Lee,
848 Functional Genomics Shared Resource, Human Immune Monitoring Shared Resource and Kimberly
849 Jordan, and the Cell Technologies Shared Resource for their support of these studies. Imaging was
850 performed in the Advanced Light Microscopy Core facility of the NeuroTechnology Center at the
851 University of Colorado Anschutz Medical Campus, which is supported in part by Diabetes Research
852 Center Grant P30DK116073. We would also like to thank Lianne Kraemer, Julia Maués, and Christine
853 Hodgdon for their input and support.

854 **Authorship contribution:** Study supervision: DMC; Conception and design: DMC, MSF; Data
855 acquisition, analysis, resources: DMC, MSF, JAJ, RAM, KLFA, MJC, TCP, ENB, SNK, PK, NJS, CAS,
856 EAW. All authors contributed to writing and approved manuscript.

857 **Competing Interests:** MSF, JAJ, RAM, KLFA, MJC, TCP, ENB, SNK, NJS, CAS, EAW: no conflicts.
858 DMC: Research grant support from Nuvation. PK: Clinical research grant support from Genentech,
859 Menarini, Eli Lilly, AstraZeneca.

860 **FIGURE LEGENDS**

861 **Fig. 1: ER+ PDXs effectively model clinical progression of ER+ BC metastases *in vivo*. a,** A
862 cohort of BCBM from the University of Colorado Cancer Center stratified by primary tumor subtype. **b,**
863 Age distribution of ER+ BCBM patient cohort. **c,** Menopausal status of ER+ BCBM patient cohort. **d,**
864 Frequency of metastasis in brain, bone, liver, and lungs for ER+ PDXs upon intracardiac injection in
865 young mice supplemented with E2 (n=10 per cell line). **e**, UCD65 GFPLuc+ cells were injected
866 intracardially into NSG mice that were i) young OVX (n=14), ii) young OVX+E2 (n=13), or III) aged
867 sham (n=13). **f,** Log-transformed extracranial metastatic burden over time, measured by IVIS. **g,** Log-
868 transformed head metastatic burden over time, measured by IVIS. **h,** Histological quantification BCBM
869 micrometastases and total clusters. Analyzed by Kruskal-Wallis and Dunn's tests. **i,** UCD65 GFPLuc+
870 cells were injected intracardially into aged female NSG mice that were i) OVX (n=12) or ii) naïve (n=11).
871 **j,** Log-transformed extracranial metastatic burden over time, measured by IVIS. **k,** Log-transformed
872 head metastatic burden over time, measured by IVIS. **l,** Histological quantification of BCBM
873 micrometastases and clusters. Analyzed by t-test. **m,** High-resolution fast spin echo T2-MRI (axial
874 planes at 9.4 Tesla) of young (12 weeks) and aged (60 weeks) NSG mice that were OVX or naïve, 16
875 weeks after UCD65 GFPLuc+ intracarotid artery injection, with mask of BM. For **f,g,j,k**, lines denote
876 mean ± SEM. Data were analyzed with 2-way ANOVA or mixed-effects analysis followed by Fisher's
877 LSD test, with p-value shown for last point only. Gray dotted line denotes baseline IVIS signal from
878 tumor-free mouse.

879 **Fig. 2: FGFR1 promotes growth of ER+ BC cells in co-culture systems modeling interactions**
880 **with the brain microenvironment. a,** IHC of pFGFR1 and FGFR1 in 48 ER^+ BCBM samples (left) and
881 membrane expression mask (right) performed using the Digital Imaging Aperio algorithm for
882 membrane-expression. Right: Spearman correlation of pFGFR1 and FGFR1 membrane expression. **b,**
883 BM frequency, FGFR amplification status, and FGFR1 relative mRNA (FPKM) for ER+ cells. **c,** FGFR1
884 and pFGFR1 immunoblots in ER+ BC cell lines. **d,** FGFR1 immunoblot in shNC and shFGFR1 UCD65
885 and UCD12 cells. Numbers indicate GAPDH-normalized expression relative to shNC, bars indicate
886 100kDa and 150kDa. Time course growth of shNC and shFGFR1 UCD65 (**e**) and UCD12 cells (**f**, n=10

887 replicates per condition) in E2-free media, treated with vehicle (EtOH) or 10nM E2. Confluence
888 measured via Incucyte imaging every 12 hours, normalized to time 0. **g,** Schematic of organotypic
889 coculture. UCD65 (**h,** n=12-17) and UCD12 (**i,** n=18-19) spheroid growth on young (9-13w) organotypic
890 brain slices; UCD65 (**j,** n=7-8) and UCD12 (**k,** n=15-16) spheroid growth on aged (49-53w) organotypic
891 brain slices. Graphs show change in GFP intensity per spheroid over time corrected for background
892 fluorescence, normalized to day 1. **l,** FGFR1 immunoblot in MCF7 FGFR1-OE and EV cells. **m,** Fold
893 change growth measured by SRB assay of MCF7 FGFR1-OE and EV cells after 6 days of treatment
894 with 10nM E2 or EtOH vehicle (n=15 replicates per condition). Growth of MCF7 spheroids (n=15-18) on
895 organotypic slices from a young (13w) (**n**) or aged (45w) (**o**) NSG mouse. For **e,f,h-k,n,o**, lines denote
896 mean ± SEM and data were analyzed with 2-way ANOVA followed by Fisher's LSD test. Data in **m**
897 were analyzed by 1-way ANOVA with Fisher's LSD test. All scale bars are 500μm. *:p<0.05

898 **Fig. 3: FGFR1 knockdown decreases ER+ BC brain metastasis in multiple models *in vivo*. a,**
899 shNC (n=12) and shFGFR1 (n=12) UCD65 GFPLuc+ cells were injected intracardially into young
900 (<14w) NSG mice that were OVX+E2. **b,** Log-transformed head metastatic burden over time, measured
901 by IVIS. **c,** Quantification of metastases in brains via H&E. **d,** Log-transformed extracranial metastatic
902 burden over time, measured by IVIS. **e,** shNC and shFGFR1 (n=6-10) UCD65 GFPLuc+ cells were
903 injected intracardially into aged (>52w) naïve NSG mice. **f,** Log-transformed head metastatic burden
904 over time, measured by IVIS. **g,** Quantification of metastases in brains via IHC of GFP and PanCK. **h,**
905 Log-transformed extracranial metastatic burden over time, measured by IVIS. **i,** shEV and shFGFR1
906 (n=6-9) UCD12 GFPLuc+ cells were injected intracardially into aged (>52w) naïve NSG mice. **j,** Log-
907 transformed head metastatic burden over time, measured by IVIS. **k,** Quantification of metastases in
908 brains via H&E. **l,** Log-transformed extracranial metastatic burden over time, measured by IVIS. For
909 **b,d,f,h,j,l,** lines denote mean ± SEM. Data were analyzed with 2-way ANOVA or mixed-effects analysis
910 followed by Fisher's LSD test. P-value shown for last time point only. For **c,g,k**, data were analyzed by
911 Mann-Whitney tests. Gray dotted lines denote baseline IVIS signal from a tumor-free mouse. #: p<0.06
912 *: p<0.05, **: p<0.01, ***:p<0.001.

913 **Fig. 4: FGF/FGFR signaling decreases in the brain TME with age and E2-depletion. a,** Aged
914 (<60w) and young (<15w) NSG mice were OVX or sham operated 14 days before intracarotid-injections
915 of UCD65 cells, and brain metastases allowed to progress for six months. At endpoint animals were
916 perfused and brains harvested and sectioned for GeoMX DSP. **b,** mRNA expression in BMs were
917 measured using human whole transcriptome atlas (WTA) library from NanoString in PanCK+ regions of
918 interest (ROI). **c,** Representative image of stained tissue and PanCK+ mask. **d,** Dimension reduction by
919 UMAP of aged and young sham PanCK+ ROIs. **e,** Volcano plots of indicated pairwise comparisons of
920 aged versus young sham PanCK+ ROIs. Significantly differentially upregulated (red) and
921 downregulated (blue) genes are shown. **f,** mRNA expression in glial cells surrounding BMs was
922 measured using mouse WTA NanoString library, using BM-associated GFAP+/Iba1+ ROI. **g,**
923 Representative image of stained tissue and GFAP+/Iba1+ mask. **h,** Dimension reduction by UMAP of
924 GFAP+/Iba1+ ROIs surrounding BM from Young (OVX or sham) and Aged (OVX or sham) mice. **i,**
925 Volcano plots of indicated pairwise comparisons of differentially expressed genes. Significantly
926 differentially upregulated (red) and downregulated (blue) genes are shown. Top 9 differentially
927 expressed clusters of pathways (defined as significant GSEA signatures sharing >35% overlapping
928 genes) for comparisons between young OVX versus sham (**j**), aged OVX versus sham (**k**), and aged
929 versus young sham (**l**) were ordered by number of genesets within the cluster and named based on
930 word frequency in pathway terms. Each node represents a significant geneset, with distance and lines
931 indicating overlap of genes, size representing the number of genes within each geneset, and color
932 representing -logFDR. Repression and enrichment of these gene signatures are indicated with arrows
933 in the legends. **m,** Venn diagram of common downregulated genes in the three indicated pairwise
934 comparisons. **n,** Normalized FGF2 expression within each group (Log(Counts per Million)), analyzed
935 with empirical bayes.

936 **Fig. 5: Astrocytes promote canonical FGF2-dependent activation of FGFR1 in ER+ BC. a,** FGF2
937 ELISA from total brain, oligodendrocyte (OL), microglia, neuron, and astrocyte lysates isolated from
938 young (12 weeks) and aged (>56 weeks) female mice (n=3). **b,** FGF2 ELISA from young (mAst P0, 15
939 days *in vitro*) and aged (Aged mAst, 90 days *in vitro*) mouse primary astrocyte lysates (n=4). **c,**

940 Immunofluorescence of GFAP and FGF2 in mAst-P0 and aged-mAst. **d,** Immunofluorescence of
941 pFGFR1 in UCD65 alone or co-cultured with mAst-P0 and aged-mAst in serum-free media. Right:
942 pFGFR1 Corrected Total Cell Fluorescence in UCD65 (n=228-303 cells per group). **e**, Schematic of the
943 experimental design for co-cultures of UCD65 shEV and shFGFR1 cells with mAst-P0 or aged-mAst. **f**,
944 Fold change in total green area relative to time 0 of UCD65 shEV and shFGFR1 cells cultured alone or
945 with mAst-P0 or Aged-mAst in E2-free media (n=3 replicates per condition), measured by Incucyte. **g**,
946 Representative images at 18 days. **h,** Schematic of organotypic co-cultures with neutralizing antibodies.
947 **i,** Spheroids of GFP+ UCD12 cells (n=10 per condition) were plated on organotypic brain slices from a
948 young (8w) NSG mouse. Slices were pretreated for 24h with 1μg anti-FGF2 blocking antibody or IgG
949 control. Graph shows change in GFP intensity per spheroid over time corrected for background
950 fluorescence, normalized to day 1. For **a,b,** data were analyzed with t tests. **d** was analyzed with
951 Kruskal-Wallis test followed by Dunn's multiple comparison test. Adjusted P-value shown. For **f,i** line
952 denotes mean ±SEM, data were analyzed with 2-way ANOVA followed by Fisher's LSD test. P-values
953 shown for last time point only.

954 **Fig. 6: NCAM1 and FGF2 activate FGFR1 signaling and growth in ER+ BC. a,** UCD65 cells were
955 serum-starved and then treated with FGF2 (10ng/mL), 25nM or 250nM recombinant human NCAM1, or
956 vehicle for 10 minutes. Immunoblot shows pFGFR1, FGFR1, pAkt, Akt, pErk, ERK. GAPDH is loading
957 control. **b,** Immunoblot from UCD65 shNC and shFGFR1 cells treated with 10ng/mL FGF2, 250nM
958 NCAM1, or vehicle for 1 hour. **c,** Immunoblot from MCF7 EV and FGFR1-OE cells treated with
959 10ng/mL FGF2, 250nM NCAM1, or vehicle for 1 hour. **d-f**, Immunoblot from UCD65, UCD12, and
960 MCF7 FGFR1-OE cells pretreated with 10μM BGJ398 or vehicle for 1 hour, then treated with 10ng/mL
961 FGF2, 250nM NCAM1, or vehicle for the indicated times. **g,** Quantification of pFGFR1 immunostaining
962 in UCD65, UCD12, MCF7-FGFR1-OE, and MCF7-EV cells cultured on top of shEV or shNCAM1 SH-
963 SY5Y cells in serum-free media (n=5 replicates per condition). Graph shows pFGFR1 Intensity in GFP+
964 areas. **h,** Representative images of UCD65 cells co-cultured with shEV and shNCAM1 SH-SY5Y cells.
965 **i,** UCD65 and UCD12 cells were grown for 7 days in starvation media on coverslips in co-culture with
966 AAV5-mCherry-mAsts. IF of panCK and pFGFR1. pFGFR1 intensity was quantified within panCK+

967 ROIs (n=108-129 for UCD65, n=60-89 for UCD12). **j,** Representative images of UCD65-mAst co-
968 cultures**.** Spheroids of GFP+ UCD12 cells (n=10 per condition) were plated on organotypic brain slices
969 from aged (46w, **k**) or young (8w, **l**) NSG mice. Slices were pretreated for 24h with 1µg anti-NCAM1
970 blocking antibody or IgG control. Graph shows change in GFP intensity per spheroid over time
971 corrected for background fluorescence, normalized to day 1**.** GFP+ UCD65 (**m**) and UCD12 (**n**) cells
972 were co-cultured on transuced mAsts (n=6 per condition) for 20 days in starvation media. GFP intensity
973 was measured every two days via Incucyte. **g,i** were analyzed by one-way ANOVA followed by Fisher's
974 LSD test. **k-n** were analyzed by two-way ANOVA followed by Fisher's LSD test. p-values shown for
975 final time points.

976 **Fig. 7: NCAM1/FGFR1 drives interactions between ER+ BC and neurons. a,** RNA-sequencing
977 schematic for UCD12 and UCD65 cells in serum-free media treated with vehicle, 10ng/mL FGF2, or
978 20ug/mL NCAM1 for 24hr (n=3). **b,** Venn diagram shows unique and shared significant gene signatures
979 following FGF2 and NCAM1 treatment. **c,** Pie chart of gene signature categories differentially induced
980 by NCAM1 treatment. **d,** log(FDR) of significant neural gene signatures differentially enriched or
981 repressed following NCAM1 treatment. **e,** Immunofluorescent staining of PSD95 and Synapsin1/2 in
982 shNC and shFGFR1 UCD65 spheroids in co-culture with organotypic brain slices from aged NSG
983 female mice (>59w) for 3 days. Punctate colocalization (n=15-21 images) was quantified. 5,000 GFP+
984 shNC and shFGFR1 UCD12 (**f**) or UCD65 (**g**) cells were plated on coverslips with 315,000 primary
985 hippocampal neurons (DIV: 8) and imaged every 12 hours for 6-9 days via Incucyte. Cell migration was
986 measured and mean distance per cell within each image (n=21-36) was plotted. Right: representative
987 images of UCD65 cells. Scale bars: 20µm. **h**, 5,000 UCD12 and UCD65 cells were plated on a
988 monolayer of shEV or shNCAM1 SY5Y cells and imaged every 12 hours for 6.5 days via Incucyte. Cell
989 migration over time was measured and mean distance per cell within each image (n=96) was plotted.
990 For **e-h**, data were analyzed by 1-way ANOVA followed by Fisher's LSD test.

991 **Fig. 8: FGFR1 kinase inhibition is only effective in early BCBM. a,** pFGFR1 quantification in brain
992 disseminated UCD65 cells 5 days after intracardiac injection in young (<12w) and aged (>56w) NSG

993 mice. Graph shows average pFGFR1 intensity in GFP+ ROIs (n=8-10 images per group) corrected by
994 background (GFP-). Data analyzed by Welch's t-test. **b,** number and percentage of brain disseminated
995 cells with positive membrane pFGFR1 staining. **c,** IF staining of PanCK and pFGFR1 in brain
996 metastases from UCD65 cells in young (<15w) and aged (>60w) NSG mice, 6 months post-intracarotid
997 injection. **d,** UCD65 GFPLuc+ cells were injected intracardially into OVX young (<18w) NSG mice
998 treated with E2 and randomized to receive vehicle (1% CMC, n=11) or BGJ398 (30mg/kg) 5x/week PO
999 starting at the time of injection (W0-12, n=9) or 7 weeks post-ic (W7-12, n=11). **e,** Log-transformed
1000 head metastatic burden over time measured by IVIS. **f,** Log-transformed *ex vivo* brain metastatic
1001 burden at endpoint, measured by IVIS and images of all brains. **g,** Quantification of metastases in
1002 brains via H&E. **h,** Representative H&E stains of metastases from two animals per group. **i,** UCD65
1003 GFPLuc+ cells were injected intracardially into aged (>52w) NSG mice and mice randomized to receive
1004 vehicle (1% CMC, n=9) or BGJ398 (30mg/kg) 5x/week PO starting at the time of injection (W0-14, n=9)
1005 or 10 weeks post-injection (W10-14, n=9). **j,** Log-transformed head metastatic burden measured by
1006 IVIS. **k,** Log-tranformed *ex vivo* brain metastatic burden at endpoint, measured by IVIS. **l,** Quantification
1007 of metastases in brains via H&E. **m,** schematic of proposed pathway. For **e,j,** data were analyzed with
1008 2-way ANOVA or mixed-effects analysis followed by Fisher's LSD test. Significant p-values shown for
1009 last time point only. Gray dotted line denotes baseline IVIS signal from a tumor-free mouse. For **f,k,l,**
1010 data were analyzed with 1-way ANOVA followed by Fisher's LSD test. Data in **g** were analyzed by
1011 Kruskal-Wallis and uncorrected Dunn's tests.

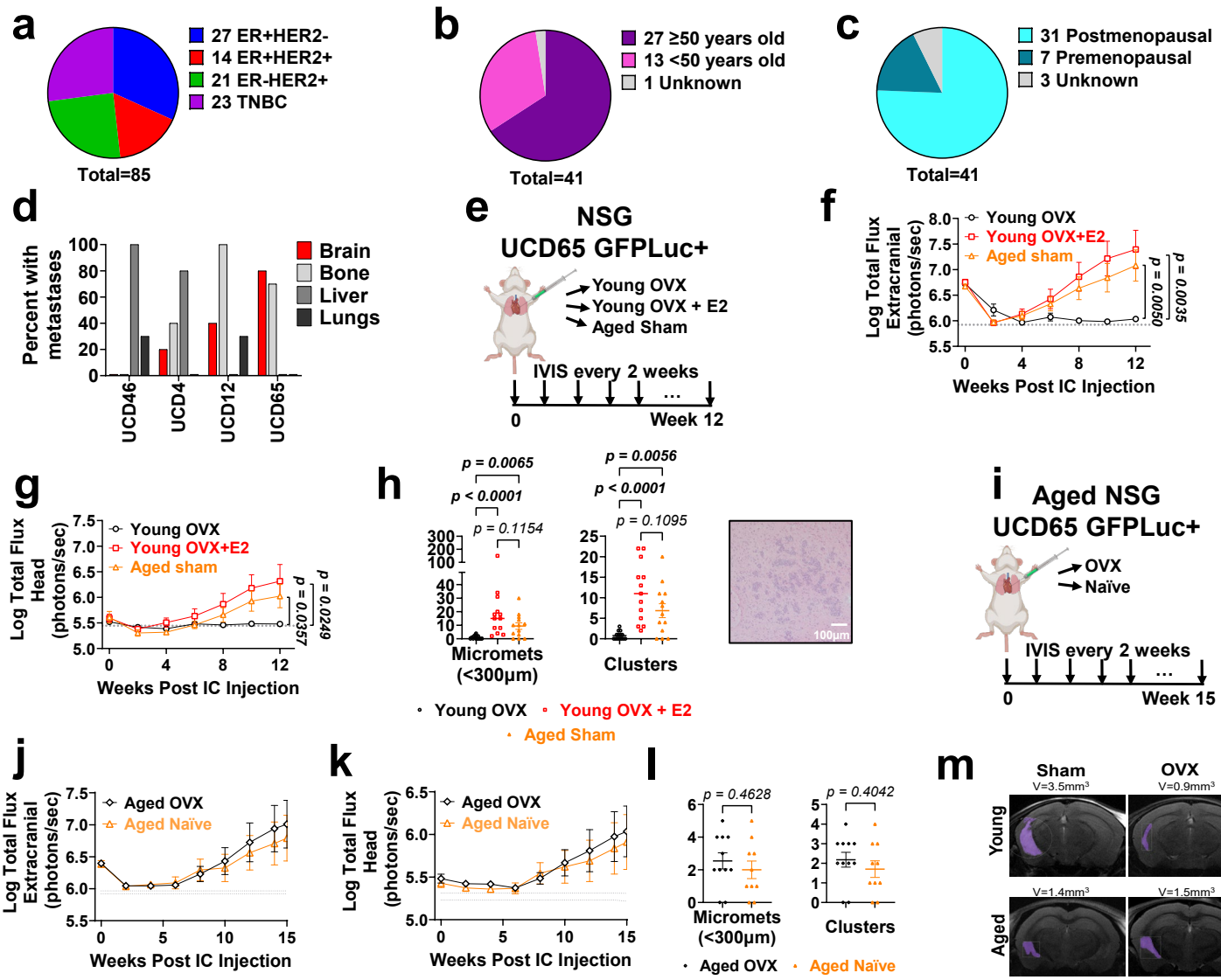
a
27 ER+HER2-
14 ER+HER2+
21 ER-HER2+
23 TNBC
Total=85
b
27 ≥50 years old
13 <50 years old
1 Unknown
Total=41
c
31 Postmenopausal
7 Premenopausal
3 Unknown
Total=41
d
Percent with metastases
Brain
Bone
Liver
Lungs
UCD46
UCD4
UCD12
UCD65
e
NSG
UCD65 GFPLuc+
Young OVX
Young OVX + E2
Aged Sham
IVIS every 2 weeks
0
Week 12
f
Log Total Flux Extracranial (photons/sec)
Young OVX
Young OVX+E2
Aged sham
p = 0.0050
p = 0.0035
Weeks Post IC Injection
g
Log Total Flux Head (photons/sec)
Young OVX
Young OVX+E2
Aged sham
p = 0.0357
p = 0.0249
Weeks Post IC Injection
h
p = 0.0065
p < 0.0001
p = 0.1154
p = 0.0056
p < 0.0001
p = 0.1095
Micromets (<300µm)
Clusters
100µm
Young OVX
Young OVX + E2
Aged Sham
i
Aged NSG
UCD65 GFPLuc+
OVX
Naïve
IVIS every 2 weeks
0
Week 15
j
Log Total Flux Extracranial (photons/sec)
Aged OVX
Aged Naïve
Weeks Post IC Injection
k
Log Total Flux Head (photons/sec)
Aged OVX
Aged Naïve
Weeks Post IC Injection
l
p = 0.4628
p = 0.4042
Micromets (<300µm)
Clusters
Aged OVX
Aged Naïve
m
Sham
OVX
V=3.5mm³
V=0.9mm³
Young
V=1.4mm³
V=1.5mm³
Aged

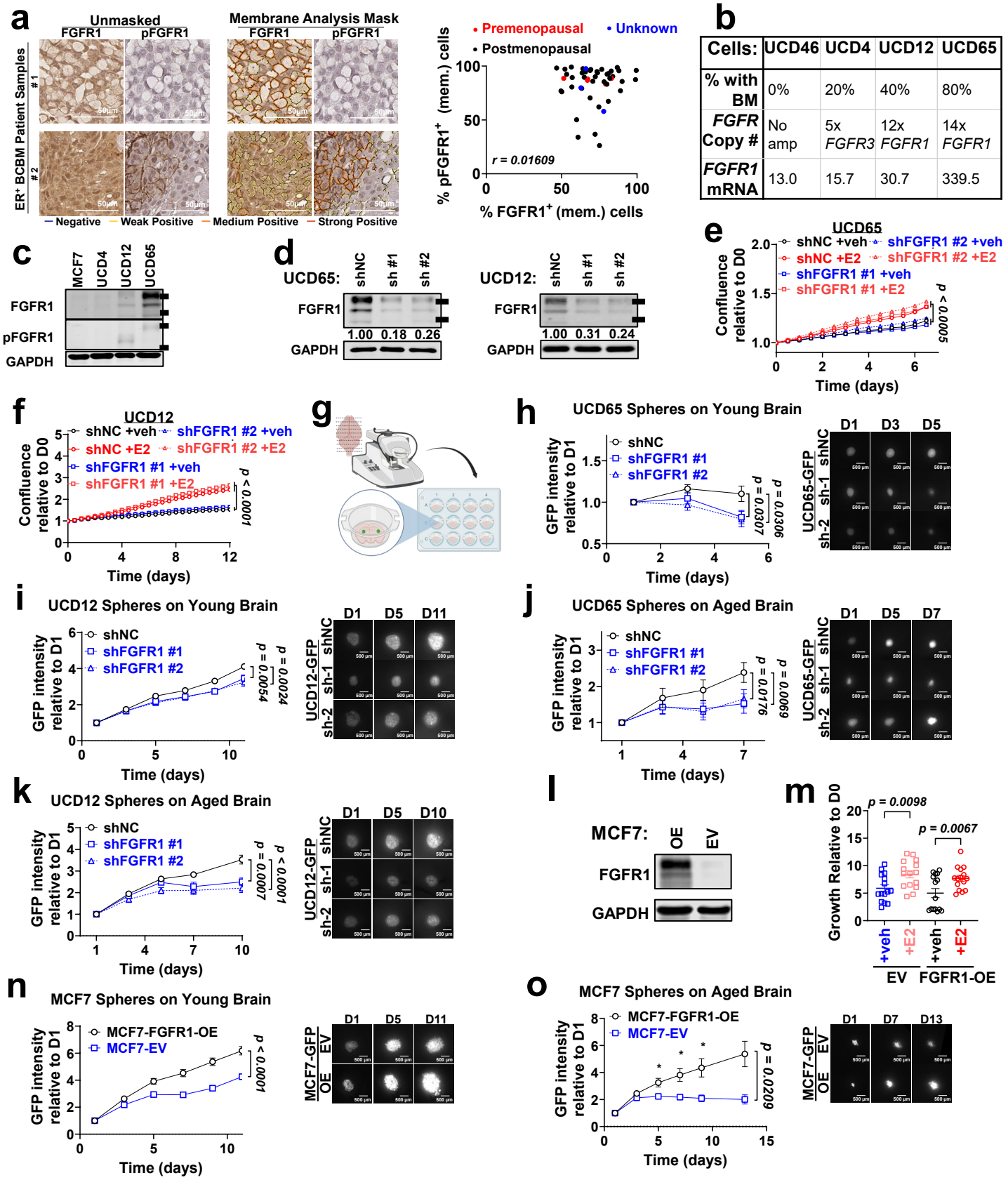

Cells:	UCD46	UCD4	UCD12	UCD65
% with BM	0%	20%	40%	80%
FGFR Copy #	No amp	5x *FGFR3*	12x *FGFR1*	14x *FGFR1*
FGFR1 mRNA	13.0	15.7	30.7	339.5

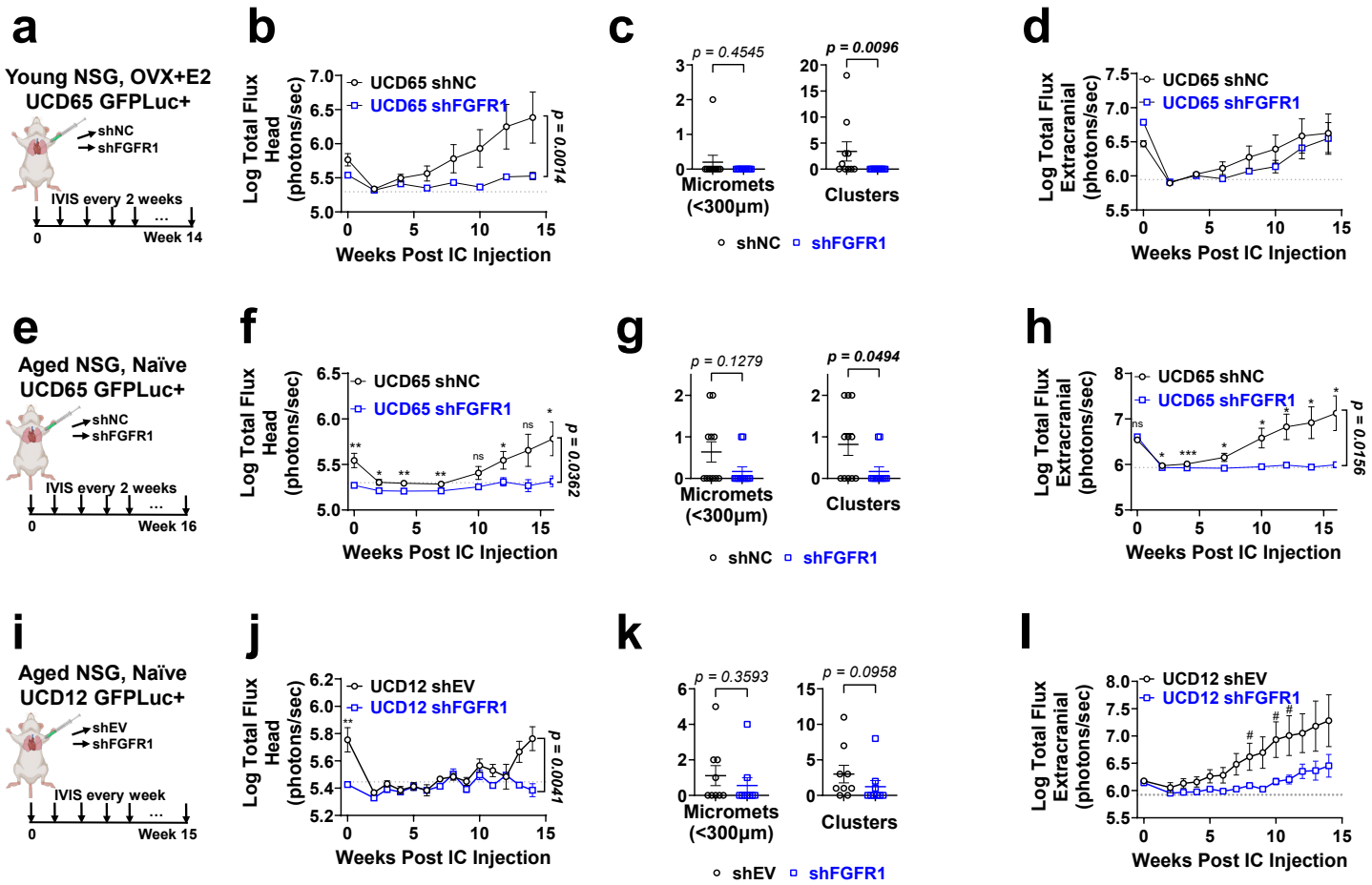
a
Young NSG, OVX+E2
UCD65 GFPLuc+
shNC
shFGFR1
IVIS every 2 weeks
0
Week 14
b
Log Total Flux Head (photons/sec)
UCD65 shNC
UCD65 shFGFR1
p = 0.0014
Weeks Post IC Injection
c
p = 0.4545
p = 0.0096
Micromets (<300µm)
Clusters
shNC
shFGFR1
d
Log Total Flux Extracranial (photons/sec)
UCD65 shNC
UCD65 shFGFR1
Weeks Post IC Injection
e
Aged NSG, Naïve
UCD65 GFPLuc+
shNC
shFGFR1
IVIS every 2 weeks
0
Week 16
f
Log Total Flux Head (photons/sec)
UCD65 shNC
UCD65 shFGFR1
p = 0.0362
Weeks Post IC Injection
g
p = 0.1279
p = 0.0494
Micromets (<300µm)
Clusters
shNC
shFGFR1
h
Log Total Flux Extracranial (photons/sec)
UCD65 shNC
UCD65 shFGFR1
p = 0.0156
Weeks Post IC Injection
i
Aged NSG, Naïve
UCD12 GFPLuc+
shEV
shFGFR1
IVIS every week
0
Week 15
j
Log Total Flux Head (photons/sec)
UCD12 shEV
UCD12 shFGFR1
p = 0.0041
Weeks Post IC Injection
k
p = 0.3593
p = 0.0958
Micromets (<300µm)
Clusters
shEV
shFGFR1
l
Log Total Flux Extracranial (photons/sec)
UCD12 shEV
UCD12 shFGFR1
Weeks Post IC Injection

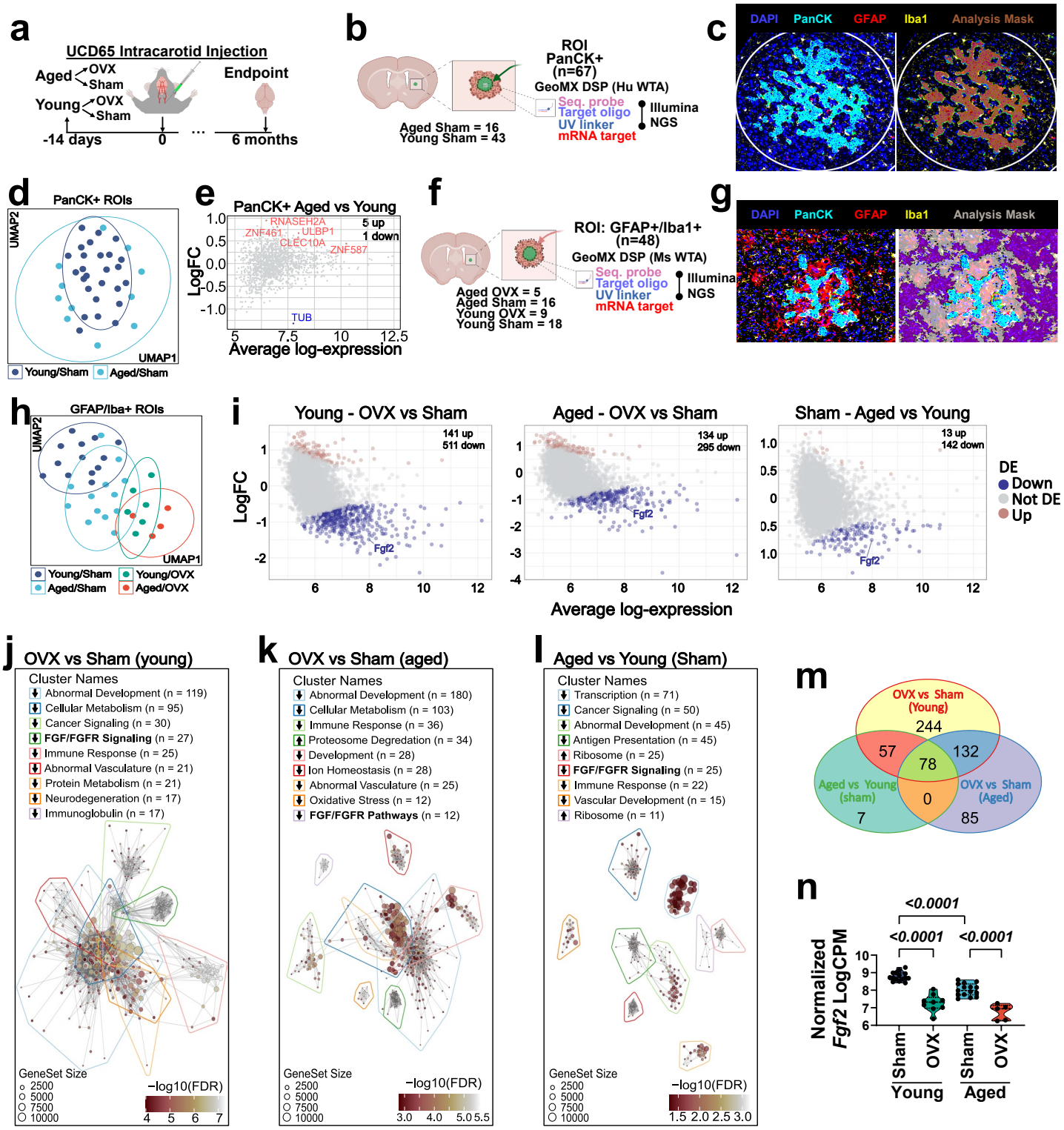
a
UCD65 Intracarotid Injection
Aged
OVX
Sham
Young
OVX
Sham
Endpoint
-14 days
0
...
6 months
b
ROI
PanCK+
(n=67)
GeoMX DSP (Hu WTA)
Seq. probe
Target oligo
UV linker
mRNA target
Illumina
NGS
Aged Sham = 16
Young Sham = 43
c
DAPI
PanCK
GFAP
Iba1
Analysis Mask
d
PanCK+ ROIs
UMAP2
UMAP1
Young/Sham
Aged/Sham
e
PanCK+ Aged vs Young
5 up
1 down
RNASEH2A
ZNF461
ULBP1
CLEC10A
ZNF587
TUB
LogFC
Average log-expression
f
ROI: GFAP+/Iba1+
(n=48)
GeoMX DSP (Ms WTA)
Seq. probe
Target oligo
UV linker
mRNA target
Illumina
NGS
Aged OVX = 5
Aged Sham = 16
Young OVX = 9
Young Sham = 18
g
DAPI
PanCK
GFAP
Iba1
Analysis Mask
h
GFAP/Iba+ ROIs
UMAP2
UMAP1
Young/Sham
Young/OVX
Aged/Sham
Aged/OVX
i
Young - OVX vs Sham
141 up
511 down
Aged - OVX vs Sham
134 up
295 down
Sham - Aged vs Young
13 up
142 down
Fgf2
LogFC
Average log-expression
DE
Down
Not DE
Up
j
OVX vs Sham (young)
Cluster Names
Abnormal Development (n = 119)
Cellular Metabolism (n = 95)
Cancer Signaling (n = 30)
FGF/FGFR Signaling (n = 27)
Immune Response (n = 25)
Abnormal Vasculature (n = 21)
Protein Metabolism (n = 21)
Neurodegeneration (n = 17)
Immunoglobulin (n = 17)
GeneSet Size
2500
5000
7500
10000
−log10(FDR)
k
OVX vs Sham (aged)
Cluster Names
Abnormal Development (n = 180)
Cellular Metabolism (n = 103)
Immune Response (n = 36)
Proteosome Degredation (n = 34)
Development (n = 28)
Ion Homeostasis (n = 28)
Abnormal Vasculature (n = 25)
Oxidative Stress (n = 12)
FGF/FGFR Pathways (n = 12)
GeneSet Size
2500
5000
7500
10000
−log10(FDR)
l
Aged vs Young (Sham)
Cluster Names
Transcription (n = 71)
Cancer Signaling (n = 50)
Abnormal Development (n = 45)
Antigen Presentation (n = 45)
Ribosome (n = 25)
FGF/FGFR Signaling (n = 25)
Immune Response (n = 22)
Vascular Development (n = 15)
Ribosome (n = 11)
GeneSet Size
2500
5000
7500
10000
−log10(FDR)
m
OVX vs Sham (Young)
244
57
132
78
Aged vs Young (sham)
0
OVX vs Sham (Aged)
7
85
n
<0.0001
<0.0001
<0.0001
Normalized Fgf2 LogCPM
Sham
OVX
Sham
OVX
Young
Aged

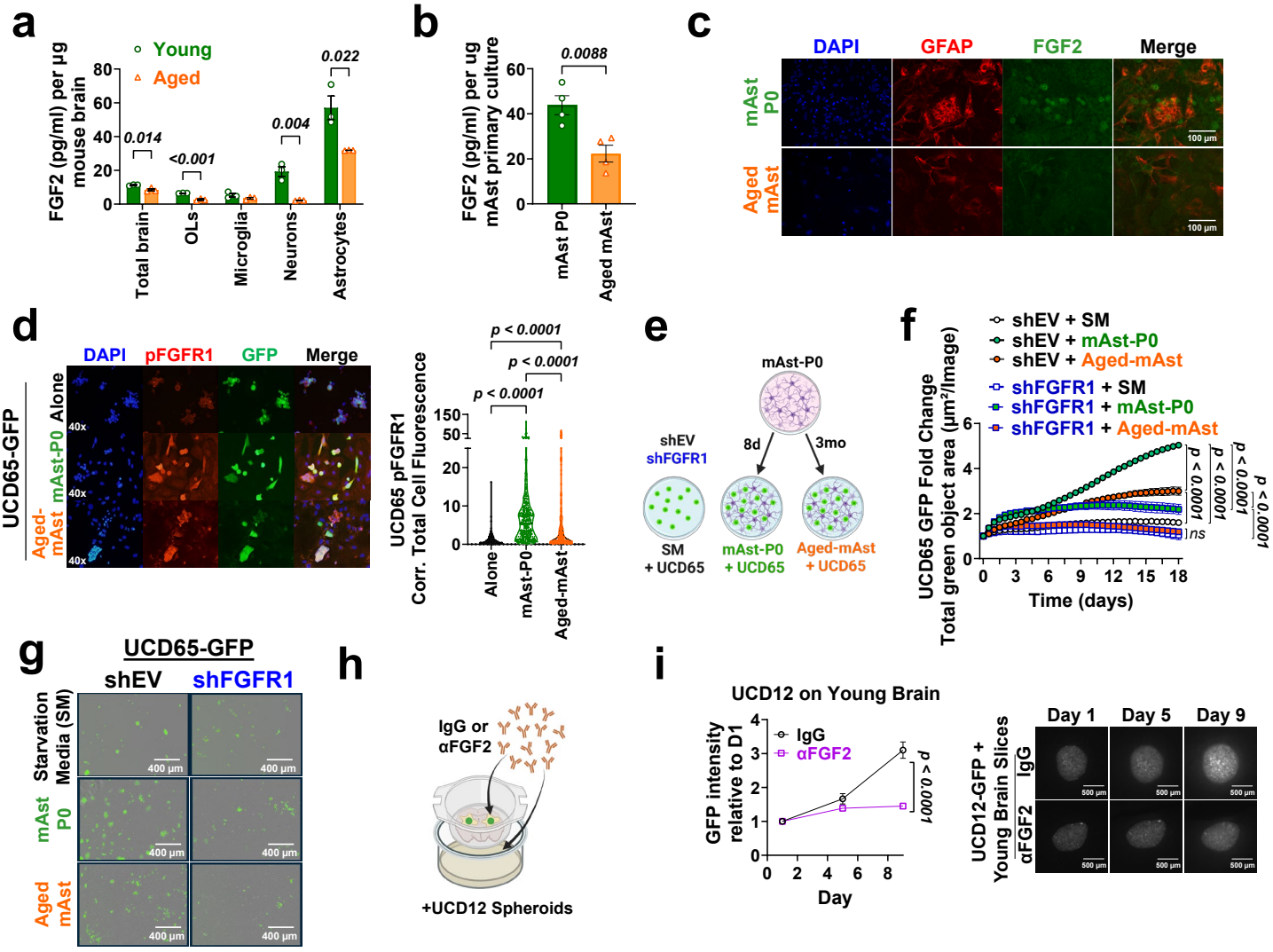
a
Young
Aged
FGF2 (pg/ml) per µg mouse brain
0.014
<0.001
0.004
0.022
Total brain
OLs
Microglia
Neurons
Astrocytes
b
FGF2 (pg/ml) per ug mAst primary culture
0.0088
mAst P0
Aged mAst
c
DAPI
GFAP
FGF2
Merge
mAst P0
Aged mAst
100 µm
d
UCD65-GFP
DAPI
pFGFR1
GFP
Merge
Alone
mAst-P0
Aged-mAst
40x
UCD65 pFGFR1 Corr. Total Cell Fluorescence
p < 0.0001
e
mAst-P0
shEV
shFGFR1
8d
3mo
SM + UCD65
mAst-P0 + UCD65
Aged-mAst + UCD65
f
shEV + SM
shEV + mAst-P0
shEV + Aged-mAst
shFGFR1 + SM
shFGFR1 + mAst-P0
shFGFR1 + Aged-mAst
UCD65 GFP Fold Change Total green object area (µm²/Image)
Time (days)
ns
g
UCD65-GFP
shEV
shFGFR1
Starvation Media (SM)
mAst P0
Aged mAst
400 µm
h
IgG or αFGF2
+UCD12 Spheroids
i
UCD12 on Young Brain
IgG
αFGF2
GFP intensity relative to D1
Day
p < 0.0001
UCD12-GFP + Young Brain Slices
Day 1
Day 5
Day 9
500 µm

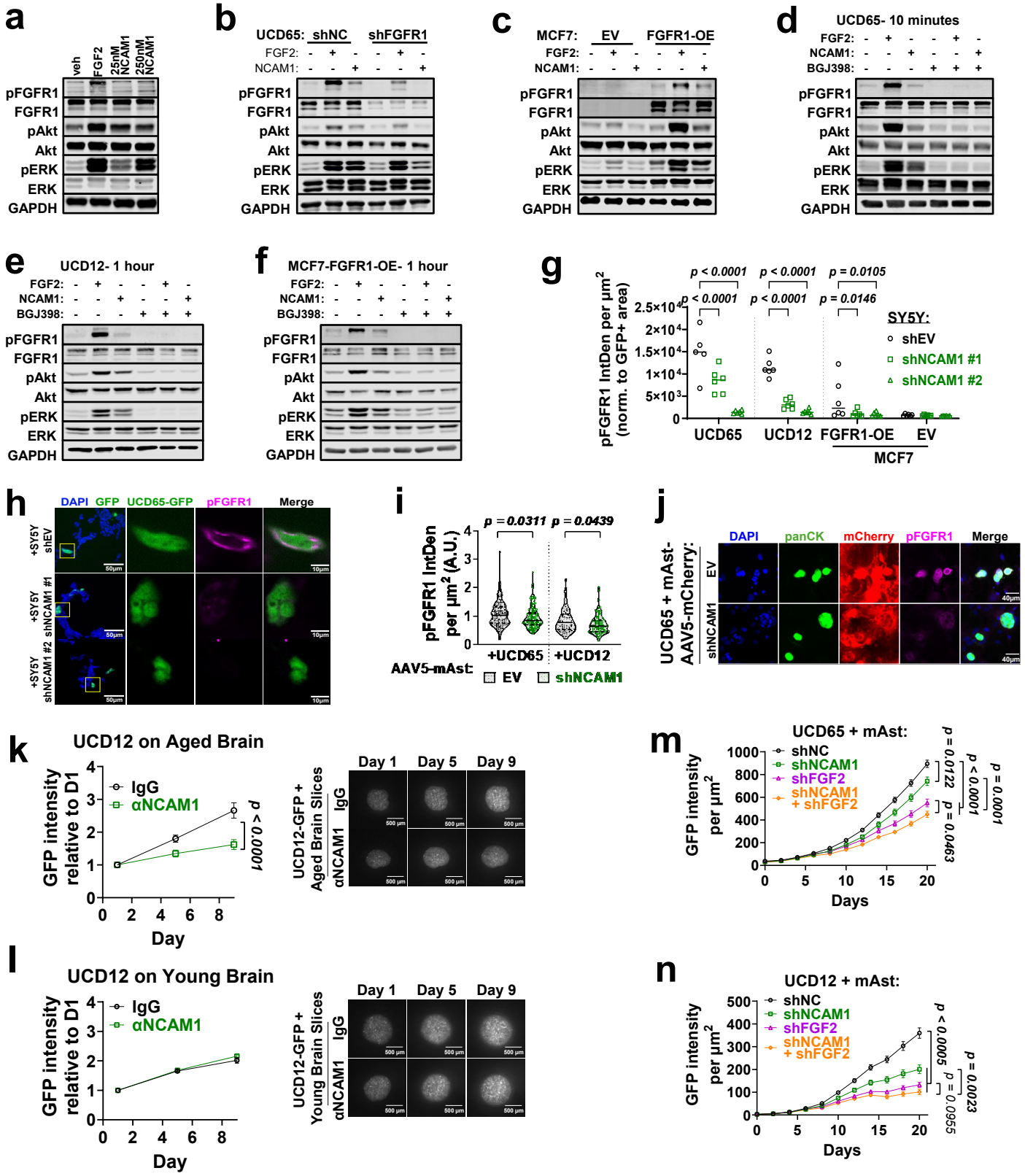
a
veh
FGF2
25nM NCAM1
250nM NCAM1
pFGFR1
FGFR1
pAkt
Akt
pERK
ERK
GAPDH
b
UCD65: shNC shFGFR1
FGF2:
NCAM1:
c
MCF7: EV FGFR1-OE
d
UCD65- 10 minutes
BGJ398:
e
UCD12- 1 hour
f
MCF7-FGFR1-OE- 1 hour
g
pFGFR1 IntDen per µm² (norm. to GFP+ area)
p < 0.0001
p < 0.0001
p = 0.0105
p < 0.0001
p < 0.0001
p = 0.0146
SY5Y:
shEV
shNCAM1 #1
shNCAM1 #2
UCD65
UCD12
FGFR1-OE
EV
MCF7
h
DAPI
GFP
UCD65-GFP
pFGFR1
Merge
+SY5Y shEV
+SY5Y shNCAM1 #1
+SY5Y shNCAM1 #2
i
pFGFR1 IntDen per µm² (A.U.)
p = 0.0311
p = 0.0439
+UCD65
+UCD12
AAV5-mAst:
EV
shNCAM1
j
UCD65 + mAst-AAV5-mCherry:
DAPI
panCK
mCherry
pFGFR1
Merge
EV
shNCAM1
k
UCD12 on Aged Brain
GFP intensity relative to D1
IgG
αNCAM1
p < 0.0001
Day
UCD12-GFP + Aged Brain Slices
Day 1
Day 5
Day 9
IgG
αNCAM1
m
UCD65 + mAst:
GFP intensity per µm²
shNC
shNCAM1
shFGF2
shNCAM1 + shFGF2
p = 0.0122
p < 0.0001
p = 0.0463
p = 0.0001
Days
l
UCD12 on Young Brain
GFP intensity relative to D1
IgG
αNCAM1
Day
UCD12-GFP + Young Brain Slices
Day 1
Day 5
Day 9
IgG
αNCAM1
n
UCD12 + mAst:
GFP intensity per µm²
shNC
shNCAM1
shFGF2
shNCAM1 + shFGF2
p < 0.0005
p = 0.0955
p = 0.0023
Days

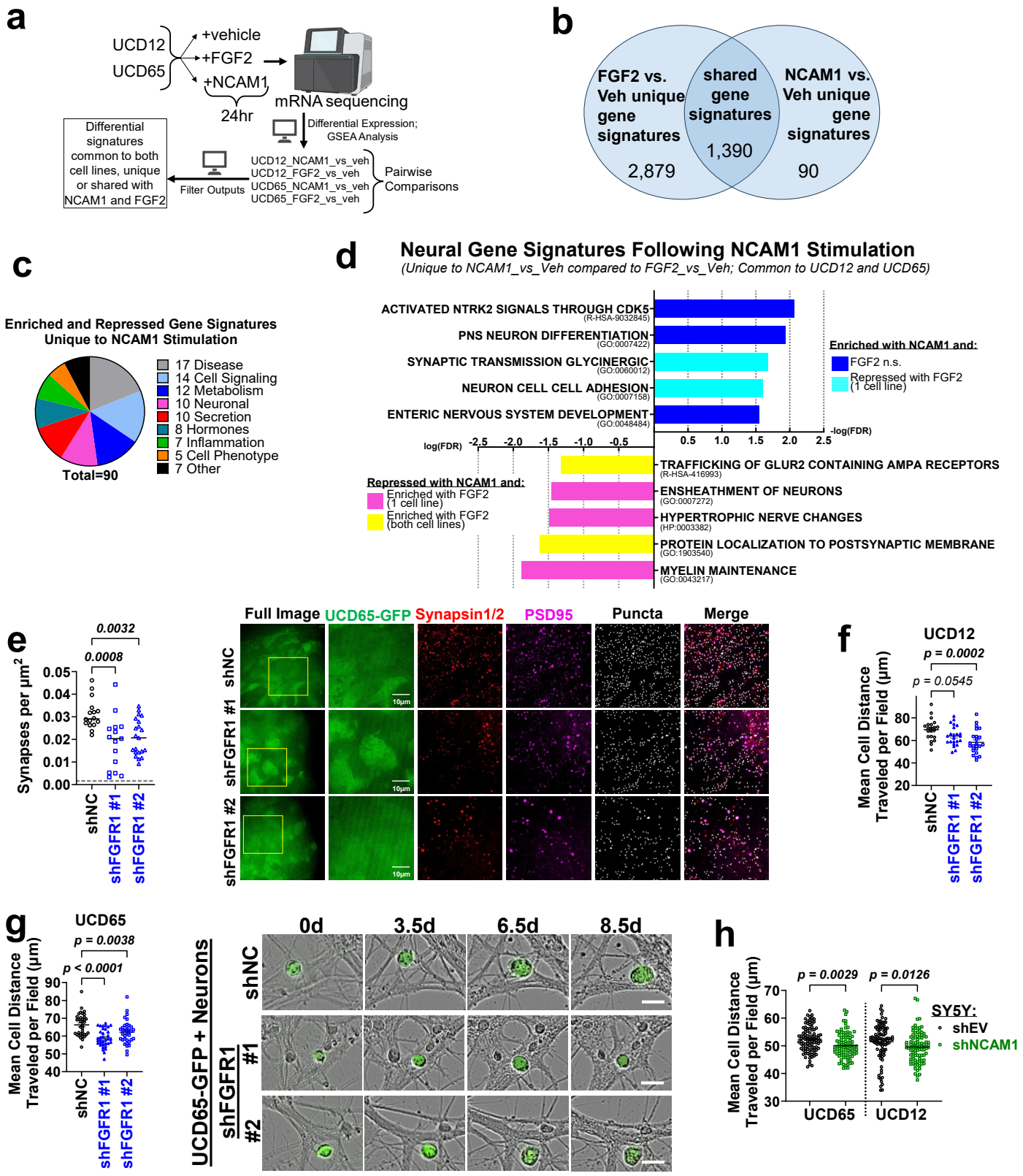
a
UCD12
UCD65
+vehicle
+FGF2
+NCAM1
24hr
mRNA sequencing
Differential Expression; GSEA Analysis
UCD12_NCAM1_vs_veh
UCD12_FGF2_vs_veh
UCD65_NCAM1_vs_veh
UCD65_FGF2_vs_veh
Pairwise Comparisons
Filter Outputs
Differential signatures common to both cell lines, unique or shared with NCAM1 and FGF2
b
FGF2 vs. Veh unique gene signatures
2,879
shared gene signatures
1,390
NCAM1 vs. Veh unique gene signatures
90
c
Enriched and Repressed Gene Signatures Unique to NCAM1 Stimulation
17 Disease
14 Cell Signaling
12 Metabolism
10 Neuronal
10 Secretion
8 Hormones
7 Inflammation
5 Cell Phenotype
7 Other
Total=90
d
Neural Gene Signatures Following NCAM1 Stimulation
(Unique to NCAM1_vs_Veh compared to FGF2_vs_Veh; Common to UCD12 and UCD65)
ACTIVATED NTRK2 SIGNALS THROUGH CDK5 (R-HSA-9032845)
PNS NEURON DIFFERENTIATION (GO:0007422)
SYNAPTIC TRANSMISSION GLYCINERGIC (GO:0060012)
NEURON CELL CELL ADHESION (GO:0007158)
ENTERIC NERVOUS SYSTEM DEVELOPMENT (GO:0048484)
Enriched with NCAM1 and:
FGF2 n.s.
Repressed with FGF2 (1 cell line)
-log(FDR)
log(FDR)
TRAFFICKING OF GLUR2 CONTAINING AMPA RECEPTORS (R-HSA-416993)
ENSHEATHMENT OF NEURONS (GO:0007272)
HYPERTROPHIC NERVE CHANGES (HP:0003382)
PROTEIN LOCALIZATION TO POSTSYNAPTIC MEMBRANE (GO:1903540)
MYELIN MAINTENANCE (GO:0043217)
Repressed with NCAM1 and:
Enriched with FGF2 (1 cell line)
Enriched with FGF2 (both cell lines)
e
Synapses per µm²
0.0032
0.0008
shNC
shFGFR1 #1
shFGFR1 #2
Full Image
UCD65-GFP
Synapsin1/2
PSD95
Puncta
Merge
10µm
f
UCD12
p = 0.0002
p = 0.0545
Mean Cell Distance Traveled per Field (µm)
g
UCD65
p = 0.0038
p < 0.0001
0d
3.5d
6.5d
8.5d
UCD65-GFP + Neurons
h
p = 0.0029
p = 0.0126
SY5Y:
shEV
shNCAM1
UCD65
UCD12

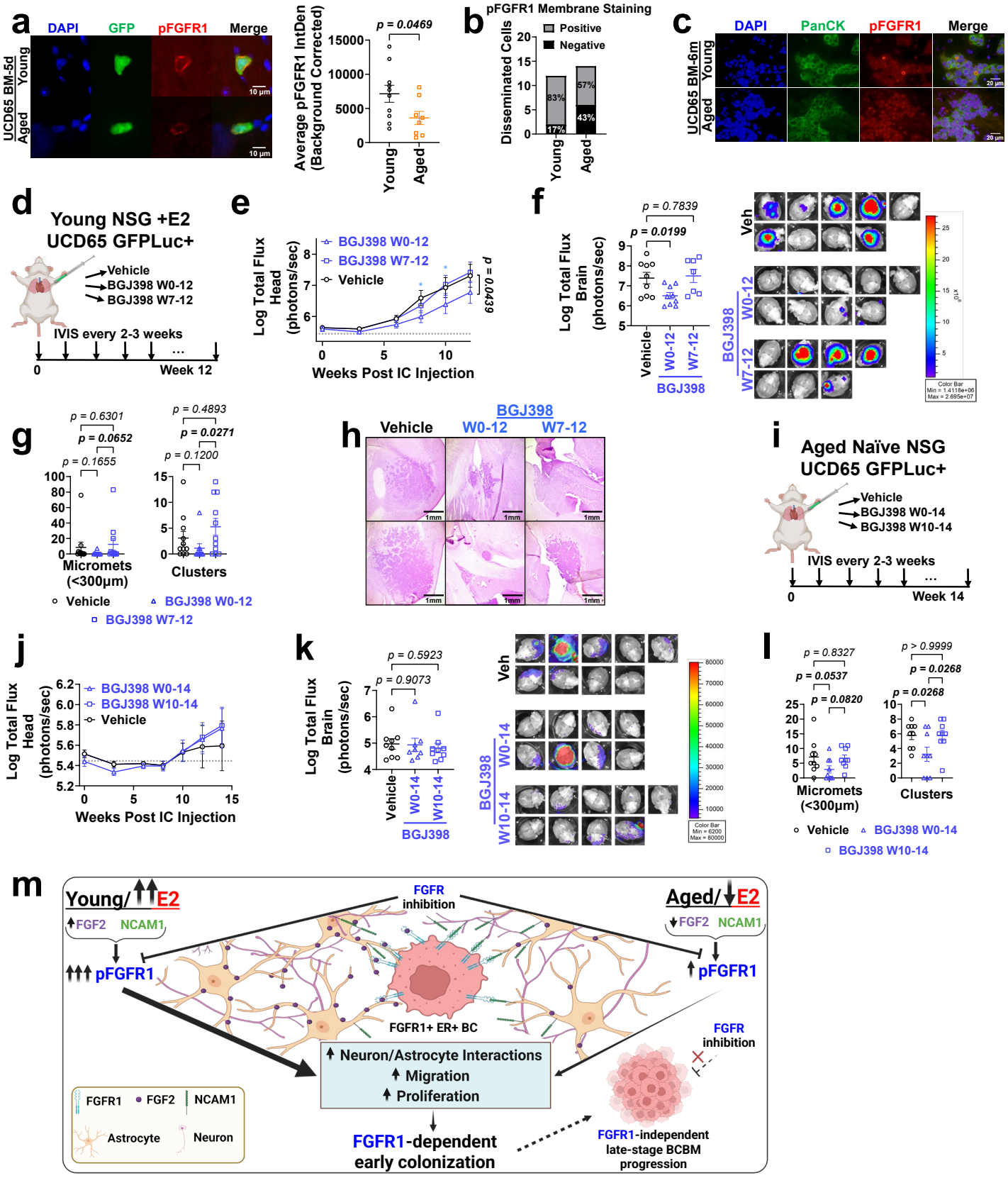
a
DAPI
GFP
pFGFR1
Merge
UCD65 BM-5d
Young
Aged
10 µm
Average pFGFR1 IntDen (Background Corrected)
p = 0.0469
Young
Aged
b
pFGFR1 Membrane Staining
Positive
Negative
Disseminated Cells
83%
17%
57%
43%
Young
Aged
c
DAPI
PanCK
pFGFR1
Merge
UCD65 BM-6m
Young
Aged
20 µm
d
Young NSG +E2
UCD65 GFPLuc+
Vehicle
BGJ398 W0-12
BGJ398 W7-12
IVIS every 2-3 weeks
0
Week 12
e
BGJ398 W0-12
BGJ398 W7-12
Vehicle
Log Total Flux Head (photons/sec)
p = 0.0439
Weeks Post IC Injection
f
p = 0.7839
p = 0.0199
Log Total Flux Brain (photons/sec)
Vehicle
W0-12
W7-12
BGJ398
Veh
BGJ398
W0-12
W7-12
Color Bar
Min = 1.4118e+06
Max = 2.695e+07
g
p = 0.6301
p = 0.0652
p = 0.1655
p = 0.4893
p = 0.0271
p = 0.1200
Micromets (<300µm)
Clusters
Vehicle
BGJ398 W0-12
BGJ398 W7-12
h
BGJ398
Vehicle
W0-12
W7-12
1mm
i
Aged Naïve NSG
UCD65 GFPLuc+
Vehicle
BGJ398 W0-14
BGJ398 W10-14
IVIS every 2-3 weeks
0
Week 14
j
BGJ398 W0-14
BGJ398 W10-14
Vehicle
Log Total Flux Head (photons/sec)
Weeks Post IC Injection
k
p = 0.5923
p = 0.9073
Log Total Flux Brain (photons/sec)
Vehicle
W0-14
W10-14
BGJ398
Veh
BGJ398
W0-14
W10-14
Color Bar
Min = 6200
Max = 80000
l
p = 0.8327
p = 0.0537
p = 0.0820
p > 0.9999
p = 0.0268
p = 0.0268
Micromets (<300µm)
Clusters
Vehicle
BGJ398 W0-14
BGJ398 W10-14
m
Young/ E2
FGF2
NCAM1
pFGFR1
FGFR inhibition
Aged/ E2
FGF2
NCAM1
pFGFR1
FGFR1+ ER+ BC
Neuron/Astrocyte Interactions
Migration
Proliferation
FGFR1
FGF2
NCAM1
Astrocyte
Neuron
FGFR1-dependent early colonization
FGFR inhibition
FGFR1-independent late-stage BCBM progression